scientific reports

Check for updates

OPEN

Multi-scale study on dynamic damage characteristics and energy dissipation of deep rock under thermal-hydro-mechanical coupling

Qi Ping[1,2] & Bobo Zhang[1,2]✉

The thermal-hydro-mechanical (THM) coupling and a strong mining disturbance environment all have a significant impact on deep ground engineering excavations, which increases the risk of a rock burst disaster. The independently developed THM multi-physics coupling apparatus enables replication of intricate geological conditions in engineered rock formations, with high-strain-rate compression experiments on deep-buried rock specimens being implemented through a split Hopkinson pressure bar testing platform. The fracture surface microstructure and the pore structure of the rock after impact are characterized by SEM and NMR. Results show that the dynamic stress–strain curve exhibits nonlinear behavior, accompanied by a significant 'plastic platform area.' Under the same temperature and pre-static stress, the energy time-history evolution distribution of rock in the process of dynamic compression has the characteristics of synchronous and different amplitudes. The energy reflection coefficient and energy dissipation coefficient obey a good exponential function and a Gaussian function relationship with water pressure, respectively. 'Compression-shear crushing failure → inclined shear boundary failure → fracture failure' is the development trend of the overall failure mode of rock when temperature and water pressure increase. The dynamic damage threshold is between 0.35 and 0.36. Microscopically, it shows a transformation trend of intergranular fracture, complex fracture, and transgranular fracture. NMR analysis reveals that elevated water pressure enhances the structural integrity of rock pores, accompanied by a reduction in pore dimensions and a progressive decline in overall porosity. A mechanical model of sliding microcrack propagation under THM coupling and impact load is constructed. By analyzing the variation patterns of crack initiation points under different operating conditions, the accuracy and adaptability of this model were validated.

Keywords Rock dynamics, Thermal-hydro-mechanical (THM) coupling, Energy dissipation, Dynamic crushing and damage, Pore characteristics, Dynamic stress intensity factor

Mineral resource development will eventually reach depths of kilometers due to the depletion of shallow resources. After the mineral resources enter the depth of kilometers, the difficulty of mining will increase, and the dynamic disasters and safety accidents, such as high-level rockbursts and mine earthquakes, large-scale coal and gas explosions, and water inrush, will be more frequent and hidden[1,2]. Compared with the exploitation of shallow resources, the environment faced by deep mining is more complicated, the mechanism is unclear, and it is difficult to predict and effectively control[3,4]. First of all, strong disturbance loads brought on by blasting, excavation, and extensive subsurface engineering rock mass mining are unavoidable. Secondly, the deep rock mass is subjected to high in-situ stress, which mainly comes from the tectonic stress generated by geological structure and the large vertical stress generated by the self-weight of overlying strata. At the same time, the deep underground is prone to producing great karst water pressure. As the rise of mining depth, the ground temperature under deep conditions will be higher and higher. The extraction of deep-seated coal deposits encounters challenging geological conditions, including elevated thermal gradients, heightened karst aquifer

[1]School of Civil Engineering and Architecture, Anhui University of Science and Technology, Huainan 232001, Anhui, China. [2]National Key Laboratory of Safe Mining of Deep Coal and Environmental Protection, Anhui University of Science and Technology, Huainan 232001, Anhui, China. ✉email: 1574473580@qq.com

pressures, substantial crustal stresses, and intense operational disturbances during mining activities[5,6](Fig. 1). Due to the unique environment of deep rock masses characterised by 'three high levels and one strong disturbance', the mechanical behavior is often different from the normal state. Under the influence of intense dynamic load disturbances like tunnel blasting, the deep roadway is more likely to become unstable and fail than the shallow roadway[7,8]. The deep dynamic disaster of the coal mine is the result of multi-field coupling. Several major disasters in deep mining are interrelated, interdependent, and mutually restricted, which pose serious challenges to deep underground coal mining[9,10]. The absence of comprehensive research on the dynamic mechanical characteristics of deep rock bulk with thermal-hydro-mechanical under strong disturbance loads, such as blasting excavation, has become an important technical problem. To establish a theoretical basis for stability assessment in deep underground rock engineering, this study investigates the dynamic behavior of deep rock masses under thermo-hydro-mechanical coupling effects. Furthermore, it elucidates the evolutionary patterns of multi-physical field interactions within deep geological formations subjected to intense external disturbances.

In the challenging conditions of deep underground rock engineering, substantial research has focused on analyzing how combined thermal, hydraulic, and mechanical factors influence rock behavior. Studies have particularly examined thermo-mechanical interactions, hydraulic-stress couplings, and multi-field interactions involving temperature, fluid pressure, and mechanical stresses to understand their impacts on rock behavior and mechanical characteristics[11,12]. Many previous studies have suggested that the rising temperatures will cause rock minerals to expand thermally, which will lead to thermal cracks and a reduction in the mechanical strength[13,14]. The mechanical properties and physical behavior of different rock types exhibit significant variations under temperature fluctuations, primarily attributed to differences in their mineral composition and microstructure[15]. Moreover, the mechanical characteristics of the rock sample will generally decrease as its water content and soaking period increase[16,17]. In the process of triaxial loading, the stress–strain curve of deep granite under high stress and high water pressure coupling environment shows obvious brittle characteristics, with a long yield stage and high residual strength[18]; under T-M coupling state, the porosity and fractal dimension of sandstone decrease with the rise of temperature, while the permeability decreases first and then increases[19]; Under coupled thermal–hydraulic-mechanical conditions, deep sandstone demonstrates enhanced peak stress and dynamic strain when exposed to elevated temperatures (20 °C ~ 50 °C) and controlled confining pressure[20], However, its elastic modulus initially increases but subsequently declines with rising temperature and pore water pressure. A critical thermal fracturing threshold exists between 25 °C ~ 100 °C, where strength degradation arises from combined effects of thermal fracturing, pore water pressure effects, and high-temperature water–rock interactions[21]. Existing research predominantly focuses on analyzing how temperature-seepage pressure-stress interactions affect rock mechanical behavior under static loading conditions. However, investigations into the dynamic mechanical responses and failure mechanisms of deep rock formations under coupled multi-field environmental effects remain insufficiently explored.

At present, to simulate the strong disturbance environment caused by blasting excavation and large-scale mining of deep rock mass, the commonly used devices in laboratory experiments are mainly the plate impact test device, SHPB, and drop hammer test device[22,23]. Because of the advantages of good controllability, strong practicability, and convenient operation, SHPB has gradually become a common experimental equipment for scholars at home and abroad to measure the dynamic mechanical response features of deep rock[24]. Dynamic impact tests of red sandstone under different hydraulic pressure and ground stress conditions were conducted by Jin et al.[25], who also designed a SHPB test apparatus for high hydraulic pressure and ground stress rock. Wu et al.[26]selected porous green sandstone for SHPB impact test under water-force coupling and derived a dynamic constitutive model of deep sandstone considering water-force coupling factors. Based on the SHPB device, Wang et al.[27] designed a set of water pressure loading test systems, and used the system to examine the dynamic impact coal samples' test under water pressure and static axial prestress loading environments. It is concluded that impact and high axial static load are two adverse conditions that get coals rock more easily damaged.

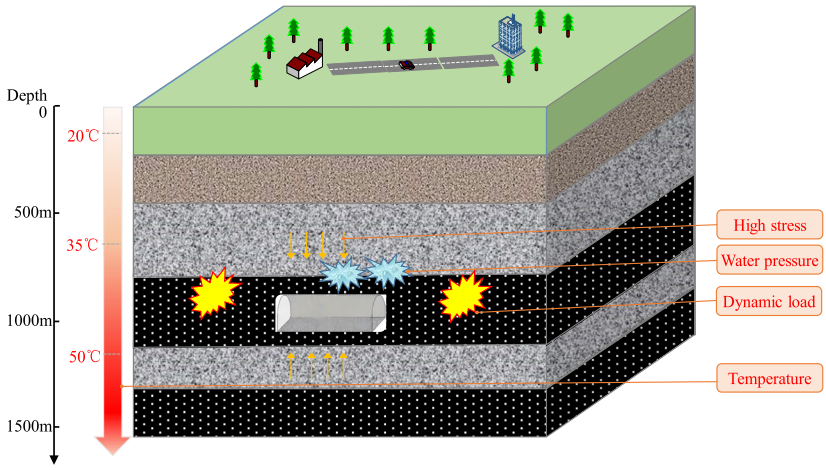

Fig.1. Disaster response characteristics of deep coal mining.

Conversely, the existence of water pressure has a positive effect on the coal, which can enhance the dynamic compressive strength. Zhao et al.[28]used the self-developed fluid–solid coupling SHPB loading system to test the deep sandstone. The findings demonstrate that as the impact rate and confining pressure increase, so does the sample's dynamic compressive strength, the impact rate has a significant impact on the cohesiveness. The above research only considers the influence of H-M coupling on the dynamic mechanical response features of rock. But in addition to causing the dynamic mechanical features of engineering rock mass to deteriorate, rising deep subsurface temperatures will also alter ground stress[29], which could significantly affect the dynamic mechanical properties. The impact of thermal-hydro-mechanical coupling on the dynamic mechanical feature of rock, however, is poorly understood. According to studies, a moderate increase in temperature will significantly alter the way that rock mechanical properties deteriorate and how microcracks propagate[30,31]. Additionally, the effect of temperature on the dynamic mechanical features of rock under temperature-water pressure-stress (THM) coupling conditions will be more complex. Consequently, it is limited to researching the effect of H-M or T-M coupling on the dynamic mechanical features of rock. Owing to the absence of multi-field coupled rock dynamics testing apparatus and varied experimental design priorities across research domains, the dynamic mechanical response patterns, fracture mechanism evolution, energy dissipation processes, and microstructural damage characteristics of rocks in high-temperature, high-seepage pressure, and high-stress coupled environments remain incompletely characterized, revealing a lack of systematic understanding in current research. In particular, the deep rock's damage and energy dissipation under dynamic load are also the focus of relevant power engineering in deep coal mining[32,33]. For example, the key to the design of the blasting scheme is how to improve the energy utilization rate of explosives, reduce the rock breaking rate, and control the damage of the surrounding rock in the near area of blasting. Therefore, it can be known that the rational allocation of rock energy distribution and transformation under dynamic load impact and the precision control of damage state are of considerable importance for ensuring the efficient mining of coal mines. Therefore, it is crucial to further consider the introduction of temperature field, truly restore the multi-field coupling state of 'three high and one disturbance', and carry out study on the dynamic mechanical features and deformation and failure modes under the action of T-H-M coupling at the same time, to clarify the dynamic energy dissipation characteristics and structural damage characteristics of deep rock mass, and reduce rock burst disasters. Combined with damage mechanics and fracture mechanics, the relevant dynamic physical and mechanical models of THM coupling are improved.

This paper aims to understand the damage characteristics and dynamic energy change features of deep rock under the influence of THM interaction. The self-developed THM multi-field environment coupling SHPB test device is used to simulate the complex environment of engineering rock. The dynamic impact compression test is performed on the saturated sandstone as the test object in a thermal-hydro-mechanical multi-field environment. The dynamic stress–strain curve, energy evolution parameters are studied with temperature (33 °C ~ 57 °C) and water pressure (2 MPa ~ 14 MPa); The microstructure of rock fracture surface was analyzed by an electronic digital microscope, and the microstructure of fracture surface and pore structure of rock after impact were characterized by SEM and NMR. By constructing an improved slip-type micro-crack propagation mechanical model, the propagation mechanism between cracks in rock under THM coupling and impact load is explored. Through the research of this paper, it is anticipated to offer a theoretical foundation and significant point of reference for the advancement of deep engineering in the intricate geological setting of "three high and one disturbance."

Materials and methods

Sample preparation

With the average burial depth of 825 m, the test rock sample was extracted from a deep coal mine sandstone in Huainan City, Anhui Province, China. All samples come from the same homogeneous sandstone to guarantee the sample's integrity and homogeneity, and Table 1 displays the sample's mechanical and physical parameters. Based on the standard of the ISRM[34] and the Chinese rock dynamic characteristics test procedure[35], the thickness $H = 25$ mm and the outer length $D = 50$ mm of the sample, and the flatness error of the two ends is ± 0.05 mm, the complete standard rock sample is selected and placed in the vacuum saturation device. When the vacuum reaches −0.1 MPa, it is allowed to stand for 48 h to ensure complete saturation. The preparation process of the sandstone are illustrated in Fig. 2.

The mineral composition analysis and microscopic morphology observation of sandstone samples after vacuum saturation treatment were carried out by Smartlab SE X-ray diffractometer and FlexSEM 1000 SEM scanning electron microscope. Fig. 3 diaplays the XRD diffraction pattern of the samples and analyzed by XRD technology. Sample is mostly maded from quartz, potassium feldspar, hematite, plagioclase, kaolinite, and a trace quantity of clay minerals. Fig. 4 displays the rock sample's interior SEM microstructure. It can be obtained that the internal microstructure is dense, and there is no obvious natural crack.

SHPB test device

The test is conducted using the self-developed THM multi-field coupling SHPB device, and it is composed of an impact dynamic loading system, data processing system, temperature-water pressure (T-H) loading system, and

Rock	Static strength	Tensile strength	Density	Wave velocity
Sandstone	57.43 MPa	4.65 MPa	2.68 g·cm^{-3}	2880 m·s^{-1}

Table 1. Mechanical and physical parameters of sandstone.

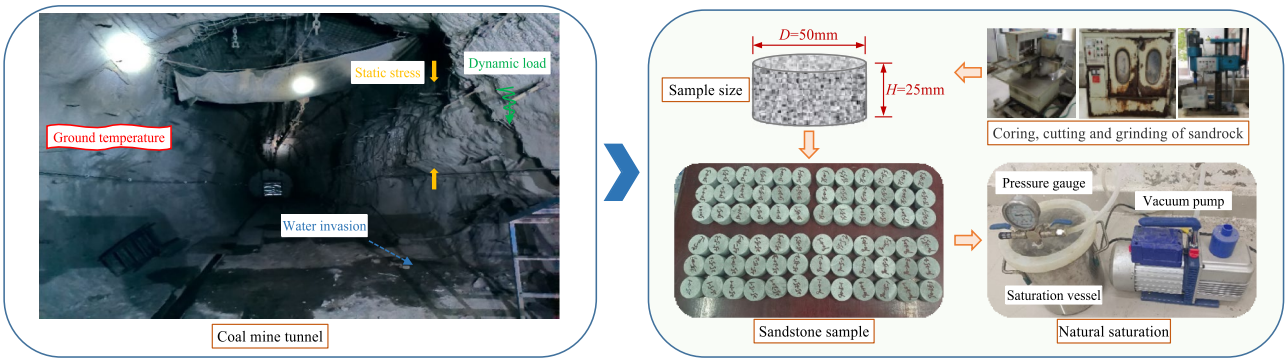

Fig.2. Sandstone sampling preparation process.

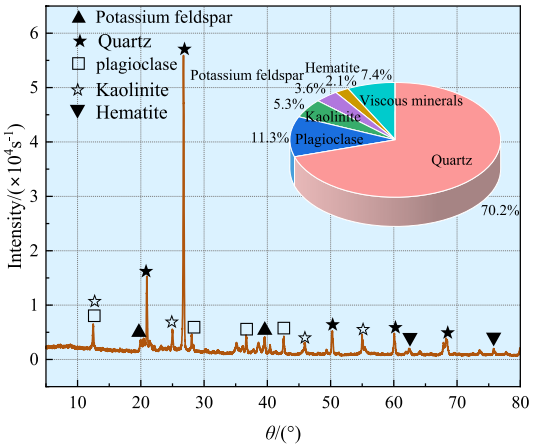

Fig. 3. XRD patterns of sandstone.

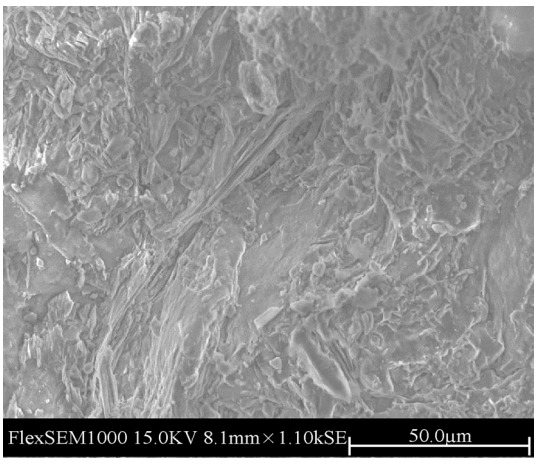

Fig.4. Microscopic morphology of sandstone.

axial static stress loading system. Fig. 5 dispalys the schematic diagram of the test device. The innovation of the device is to add a temperature-water pressure loading device and an axial static stress device to the traditional SHPB device. The temperature-water pressure loading device is associated with the high and low temperature water bath circulation box. The water medium around the deep rock is heated to the target temperature by water bath heating, so as to achieve the purpose of simulating the real geothermal environment. The water bath heating box can display the heating temperature in real time, and the water bath heating temperature range is between 0 ~ 100 °C.On the intelligent control system of axial (ring) pressure, the display controller can output

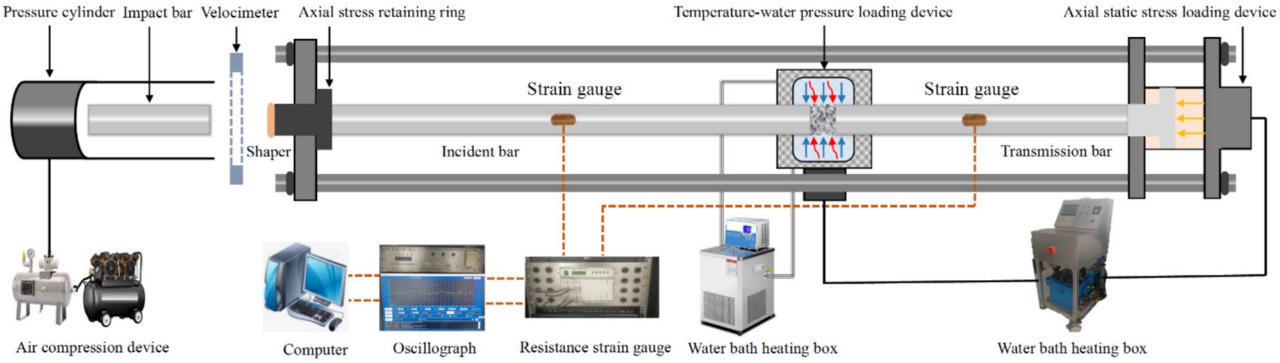

Fig.5. THM multi-field coupling Hopkinson pressure bar device schematic diagram.

oil pressure to the axial static stress loading device by controlling the oil cylinder and the hydraulic line to generate stress load, to provide high static stress to deep rock, and adjust the stress load to ensure accuracy. The stress value range is 0 ~ 40 MPa, and the axial static stress continuous maintenance function is realized during the impact process, and the display controller displays the positive axial pressure. The strong disturbance load is realized by the impact dynamic loading system, which mainly includes a frequency conversion air pressure device, an incident bar, a high-pressure cylinder, a transmission bar, an impact bar, and a laser velocimeter. The data processing system is composed of a computer, oscilloscope, and dynamic resistance strain gauge, which is in charge of processing and keeping track of the reflected, transmitted, and incident waves that the strain gauge collects.

The self-developed temperature-water pressure loading device includes a water outlet pipe, water inlet pipe, water stop valve, water pressure display, sealing cover, water stop cover, confining pressure actuator, and bearing bar. The physical diagram of the THM multi-field coupled Hopkinson pressure bar device and temperature-water pressure loading device is shown in Figs.6a and b. The main principle of water pressure device is as follows: there is heated water medium and no bubbles appear within the device, the water stop valves at the inlet and outlet are closed, the axial (ring) pressure intelligent control system controls the oil cylinder to output oil pressure to the confining pressure actuator through the hydraulic line, and adjusts the expansion amount of the bearing bar, so that the internal volume changes, so that the water pressure can be adjusted. The water pressure range is 0 ~ 25 MPa, the steady-state control accuracy is ± 1 MPa, the loading rate is controllable. The strong disturbance impact load and the axial prestress are transmitted to the deep rock through the transmission bar and the incident bar, respectively. Simultaneously, the deep rock is affected by the water pressure and temperature inside the temperature-water pressure loading device. The loading conditions of the sample are presented in Fig. 6c.

Test scheme

In Huainan City, Anhui Province, a deep coal mine's average depth is 836 m, the maximum tectonic stress is 26.8 MPa, the maximum temperature of the original rock is above 45 °C, the average geothermal gradient is 3 °C/hm, and the high water pressure is greater than 4.5 MPa[36,37]. According to existing research[38], rockburst manifests only under pre-static stresses of 25 ~ 50 MPa during dynamic rock compression. Considering the actual situation in deep rock engineering, the rock's ambient temperature is generally not exceed 100 °C. At this temperature, the temperature field can be applied by heating the sample in a water bath. Therefore, the axial pre-static stress and fixed dynamic impact velocity of the test are 26 MPa and 9 m/s. The impact velocity was captured using an infrared laser velocimeter. During testing, the impact velocity was fixed by setting a constant impact air pressure. Temperatures were set at 33 °C, 39 °C, 45 °C, 51 °C, and 57 °C, while water pressure values were set at 2 MPa, 5 MPa, 8 MPa, 11 MPa, and 14 MPa. Four parallel specimens were prepared for each group, totaling 100 specimens. It is important to remember that to decrease test error and increase test accuracy and reliability, the rock sample of the sounding part needs to be placed in a constant temperature water bath box in the corresponding heating water medium for 48 h before the test, to ensure that the rock reaches the corresponding ground temperature.

Test method

SHPB test

It is worth noting that the constant temperature water bath box is placed in front of the loading position of the SHPB test instrument bar, which is convenient for the test operation to take out the saturated sample and quickly move it into the temperature-water pressure loading device. The 30% pre-static stress is applied first to confirm that the bar is in close connect with the rock, and the sealed end cover is installed. The high and low temperature water bath circulation box heats the water medium to the target temperature in advance and transports it to the surroundings of the test sample, and then applies the pre-static stress to the set value. The water body is heated back and forth for a certain period of time and exhausts the internal air, which is convenient for applying the water pressure to the set value.

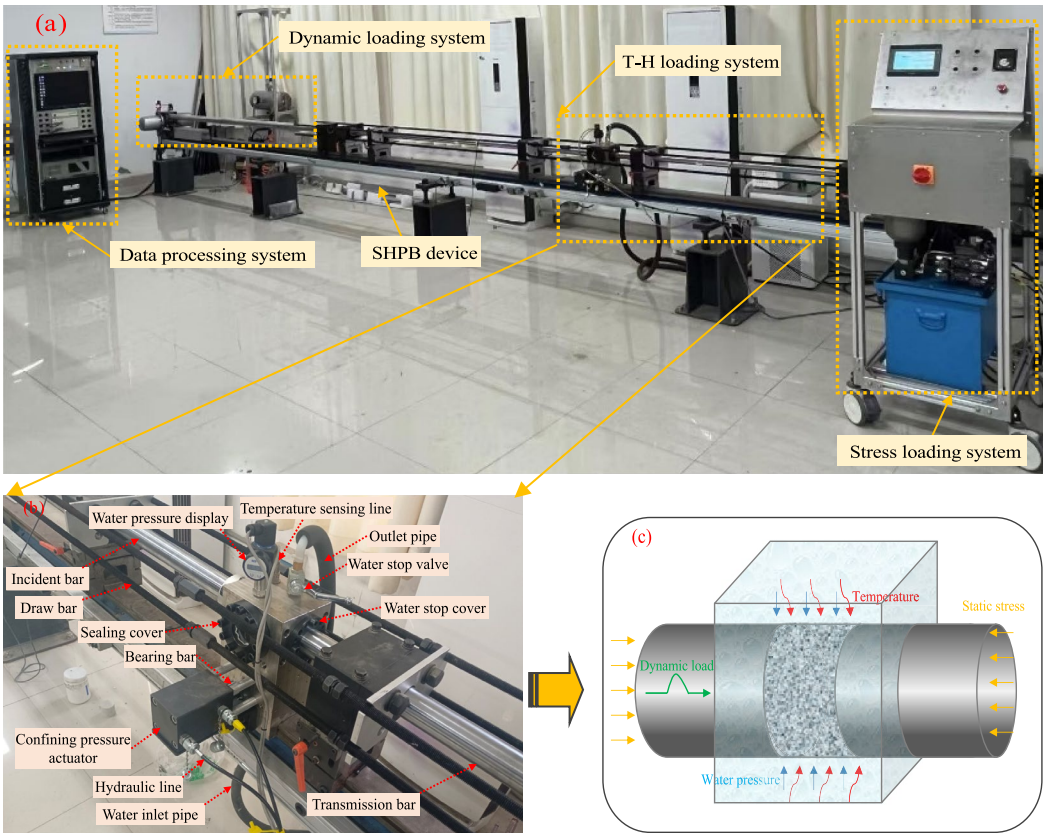

Fig.6. (**a**) THM multi-field coupling Hopkinson pressure bar device physical diagram, (**b**)Temperature-water pressure loading device, (**c**)Loading condition diagram.

Fig.7. P wave、SEM and NMR test device.

P wave test

Before testing, the P-wave velocity of samples was obtained using a seismometer. Following the test, these samples that remained intact after impact was again measured using the seismometer to characterize the dynamic damage extent of deep rock under THM coupling. The seismometer is shown in Fig. 7a.

SEM test

After the dynamic impact post-test under THM coupling, the broken test block was selected from the broken sample and made into the a size sample required for the scanning electron microscope according to the requirements, and then gold was sprayed on the IXRF Model 550i spraying instrument. The scanning test instrument is the FlexSEM1000 scanning electron microscope produced by HITACHI Company in Japan, which can be magnified 16 ~ 800,000 times, with a resolution of up to 5.0 nm, and has two electron and backscatter

imaging methods. Finally, the microstructure of granite under different working conditions is obtained. The scanning electron microscope is shown in Fig. 7b.

NMR test

The rock samples after dynamic impact under THM coupling were taken out after being saturated by the pure water vacuum method for 8 h. After taking out, the T_2 spectrum distribution test was measured in turn to acquire the pore size distribution characteristics of deep rock under different water pressure conditions. The NMR test is presented in Fig. 7c.

Stress balance verification

The effectiveness of experimental data concerning the dynamic stress and strain properties of deep rock may be assessed by examining stress equilibrium across the specimen's front and rear surfaces. Specifically, the superposition of reflected and incident waves should substantially consistent with transmitted wave. Only under conditions of stress equilibrium can the obtained 'dynamic stress–strain curve' be considered highly credible. The display controller shall show the magnitude of the forward axial compression in real time[38]. Figure 8a are typical stress wave curves of deep rock under THM coupling. Fig. 8b illustrates that the three-wave stress data have a good coincidence effect, indicating that the deep rock in the thermal-hydro-mechanical coupling environment can basically meet the requirements of stress–strain uniformity assumption during dynamic impact loading.

Test principle

The temperature, water pressure, and axial pre-stress acting upon deep rock specimens constitute static loads. Essentially, both the transmitted and incident bars adhere to the principles of one-dimensional stress wave theory. The signal wave data collected by strain gauges is processed by substituting into the 'three-wave method' equation to obtain the sample's dynamic stress, dynamic strain, and strain rate. This can be obtained from Eqs. (1) ~ (3)[39].

$$\sigma(t) = \frac{E_0 A_0}{2A_s}\left[\varepsilon_I(t) + \varepsilon_R(t) + \varepsilon_T(t)\right] \tag{1}$$

$$\varepsilon(t) = \frac{C_0}{L_s}\int_0^{\tau}\left[\varepsilon_I(t) - \varepsilon_R(t) - \varepsilon_T(t)\right]dt \tag{2}$$

$$\dot{\varepsilon}(t) = \frac{C_0}{L_s}\left[\varepsilon_I(t) - \varepsilon_R(t) - \varepsilon_T(t)\right] \tag{3}$$

In essence, the impact crushing process of deep rock under THM coupling conditions is the process of initiation, propagation, aggregation and final penetration of pore cracks in rock under energy-driven action. The incident energy Q_I, the reflected energy Q_R, and the transmitted energy Q_T can be represented as follows[40]:

$$Q_{I,R,T} = A_0 E_0 c_0 \int_0^t \varepsilon_{I,R,T}^2(t)dt \tag{4}$$

In the above equation,E_0,c_0, and A_0 are the elastic modulus (N/mm^2), wave velocity(m/s), and cross-section area(mm^2) of the bar; $\varepsilon_I(t)$,$\varepsilon_R(t)$, and $\varepsilon_T(t)$ are the strains measured on the incident bar, the reflection bar, and the transmission bar at the corresponding time;t is the stress wave duration(μs).

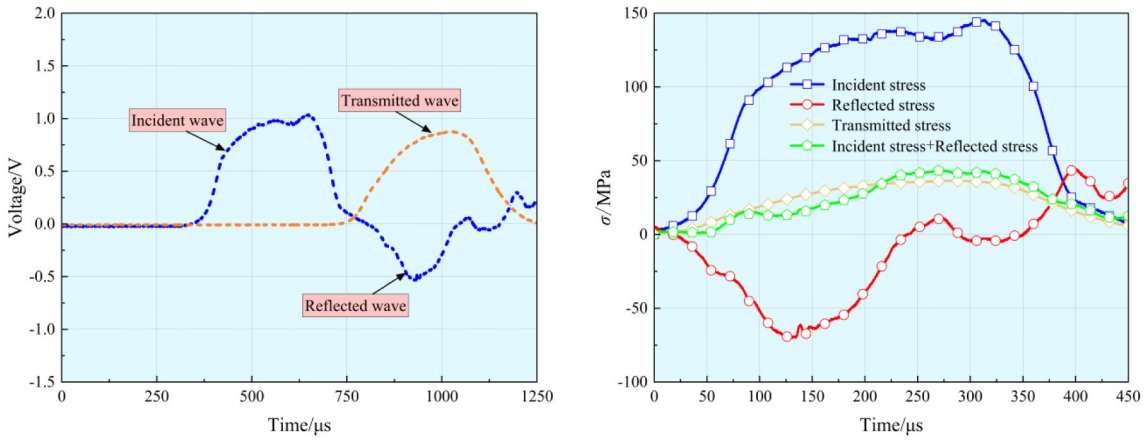

(a) (b)

Fig.8. Typical stress wave curve and dynamic stress equilibrium curve of deep rock under THM coupling.

The experimental analysis presumes the exclusion of frictional effects at the contact surfaces and disregards energy dissipation between the striking bar and elastic member, with the working hypothesis that the impactor's kinetic energy is fully transformed into incident stress wave energy. The rock dissipation energy Q_S, the energy reflection coefficient H_R, the energy transfer coefficient H_T, and the energy dissipation coefficient H_S are as follows, respectively[41,42].

$$Q_S = Q_I - Q_R - Q_T \tag{5}$$

$$H_R = \frac{Q_R}{Q_I} H_T = \frac{Q_T}{Q_I} H_S = \frac{Q_S}{Q_I} \tag{6}$$

Experimental results

Dynamic stress–strain curve

To a certain degree, the dynamic mechanical response characteristics of the sample can be described by the dynamic stress–strain curve of rock. Fig. 9 illustrates the stress–strain curve of rock under T-H-M coupling. When the water pressure and pre-static stress load remain constant, the stress–strain curves of rock under various temperatures show significant nonlinear characteristics. The three stages are as follows: elastic deformation stage (O-I stage), plastic yield stage (I-II stage), and post-peak failure stage (II-III stage).

(a) During the elastic deformation stage (O-I stage), the pores within the rock are not only filled with water but are also gradually compacted under the effects of pre-existing stress and water pressure. Under the effect of disturbing loads, the water filling the pores within the rock cannot be expelled promptly. As a result, the rock exhibits a strong compressive state under the dynamic loading process, causing the initial segment of the curve to rise approximately linearly. This stage no longer exhibits the pore compaction phase characteristic of uniaxial compression. As dynamic stress continues to increase and temperature rises, dynamic stress concentrates at microfractures within the rock and propagates forward. Microfractures that were previously compacted and closed begin to redevelop. The rate of increase on the stress–strain curve slows down and no longer exhibits a linear rise. At this point, the rock enters the I-II stage.

(b) A distinct "plastic plateau region" appears during the I-II stage. As temperature increases, thermal expansion occurs in the mineral grains within the rock. Under impact loading, the bonding strength between the cementing materials within the rock is weakened due to temperature changes and the influence of pore water pressure. Simultaneously, the specimen itself absorbs dynamic and static load energy[43], resulting in enhanced plasticity and an extended elastic–plastic stage, thereby forming the plastic plateau region. When

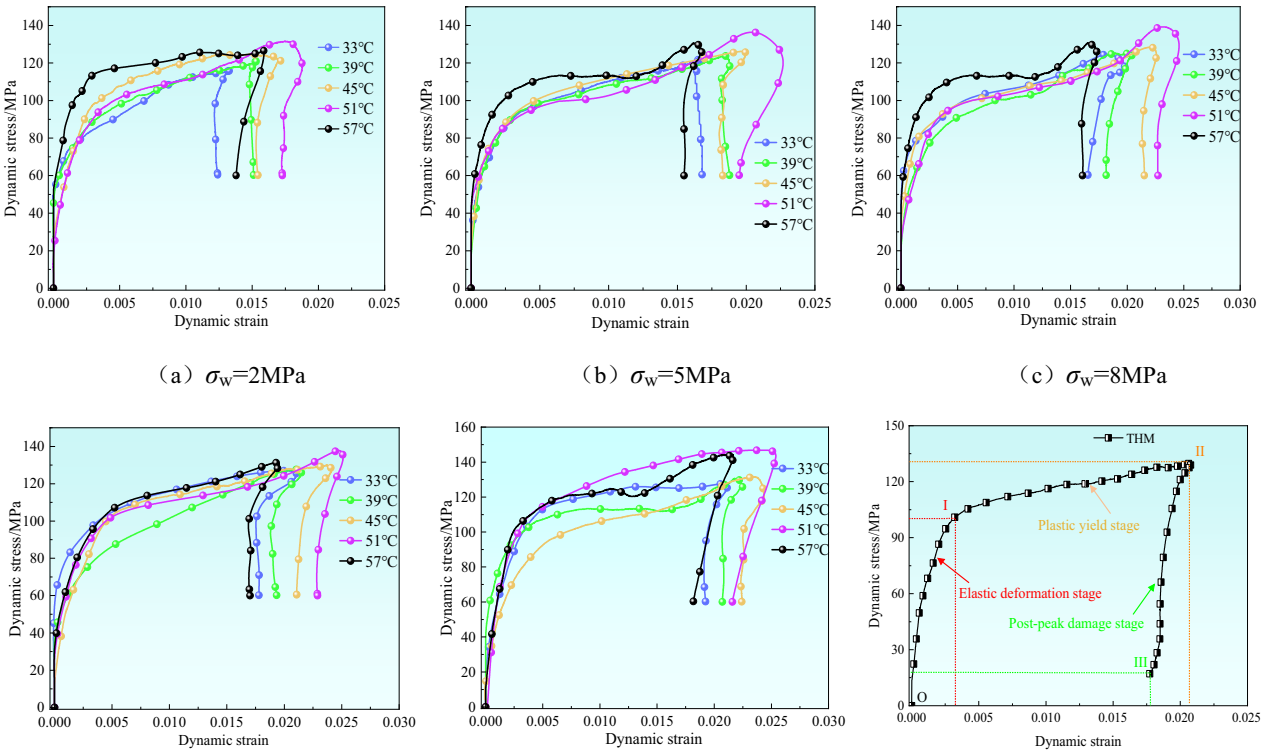

（a）σ_w=2MPa　（b）σ_w=5MPa　（c）σ_w=8MPa

（d）σ_w=11MPa　（e）σ_w=14MPa　（c）Schematic diagram of segmentation

Fig.9. Dynamic stress–strain curve changes under T-H-M coupling.

the dynamic stress–strain curve reaches its peak, the rock undergoes macroscopic instability failure and transitions from the plastic yielding stage to the II-III stage.

(c) During the II-III stage, after the dynamic strain reaches its peak value, the dynamic strain reduces slightly, and the dynamic stress decreases rapidly. The II-III stage curve exhibits distinct elastic after-effects, indicating that the rock still possesses bearing capacity, particularly within a certain temperature range and under high water pressure. In some cases, macroscopic failure does not occur in the rock, as the applied external water pressure acts as confining pressure[27]. Hydrostatic confining pressure exerts a uniformly restrictive effect on internal rock fractures, limiting radial deformation of the rock, thereby enhancing its integrity and uniformity, reducing the degree of specimen fragmentation, and altering the failure mode to exhibit higher impact resistance. Thermal expansion forces and pre-existing stress caused by temperature within a certain range may also contribute to the closure of some primary fractures, preventing further development of internal rock fractures, thereby enhancing the rock's load-bearing capacity to resist deformation.

Additionally, Fig. 9 displays that when the temperature is below 51 °C, the peak dynamic stress of deep rocks gradually increases with increasing water pressure and rising temperature. When the temperature exceeds 51 °C, the peak dynamic stress of deep rocks gradually decreases with increasing water pressure and rising temperature. This is because the continuous increase in temperature causes inconsistent thermal expansion deformation across grain boundaries within deep sandstone, generating structural thermal stress. This will lead to the production of new microcracks in deep rocks, which, to some extent, deteriorates the internal grain bonding state. As a result, the combined effects of thermal-hydro-mechanical weakened impact resistance, resulting in a gradual decline in peak dynamic stress.

Energy dissipation

Energy and stress-dissipated energy time history evolution

The energy evolution law has been widely applied in rock mechanics research and testing and is a valuable technique for examining the deformation and failure features. From a microscopic perspective, rock deformation, and failure result from the evolution of internal damage, which is created by the continuous propagation of initial defects such as microcracks. During their propagation, microcracks require energy to generate new fracture surfaces. This implies that part of the work done by outer forces on the rock is dissipated by means of microcrack propagation. This portion of energy is referred to as dissipated energy. Based on Eq. (4), the energy time history curves and stress-dissipated energy time evolution curves of deep rocks under different temperatures and water pressures can be observed. Taking the typical energy time history curves and stress-dissipated energy time evolution curves of rocks under $T = 39℃$ and $T = 51℃$ as examples for analysis, as shown in Fig. 10 and Fig. 11, the energy changes exhibit synchronous amplitude characteristics, meaning that the duration of energy action aligns with the duration of stress waves, while the amplitude of changes varies. This is specifically manifested in the following two aspects:

(1) It can be obtained from Fig. 10, the time-history curves of transmitted energy, reflected energy, and incident energy exhibit similar evolutionary characteristics, all increasing with time and eventually stabilizing at a certain level. In contrast, the time-history curve of dissipated energy shows significant differences, characterized by a brief decline after reaching its peak, with the released dissipated energy primarily converting into transmitted energy. During the initial stage of impact loading, reflected energy grows at a substantially slower rate than dissipated energy, with reflected energy being less than dissipated energy. As time progresses, reflected energy gradually exceeds dissipated energy. Additionally, dissipated energy exhibits a brief downward trend, which always occurs after the incident energy stabilizes, indicating that during this stage, secondary and primary cracks within the rock continue to expand and connect, forming an intersecting crack network. When damage accumulation reaches a critical state, energy evolution tends toward a stable value. The underlying cause can be explained as follows: under thermo-hydro-mechanical coupling, the rock sample lacks sufficient stored

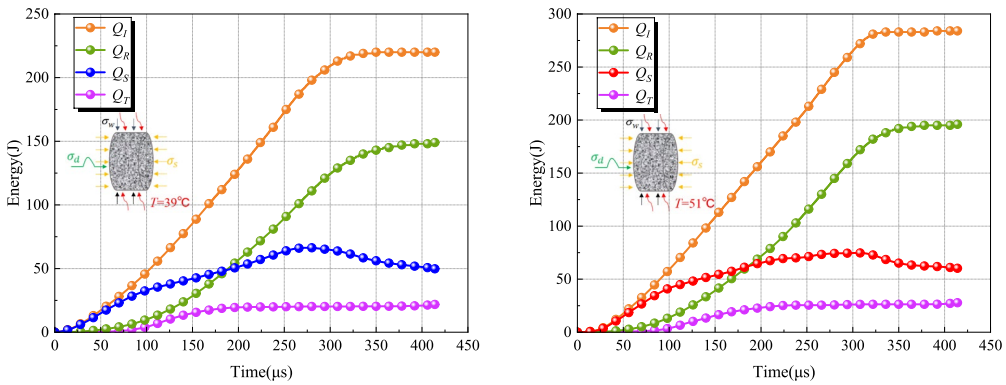

(a) T=39℃ (b) T=51℃

Fig.10. Energy time history curve.

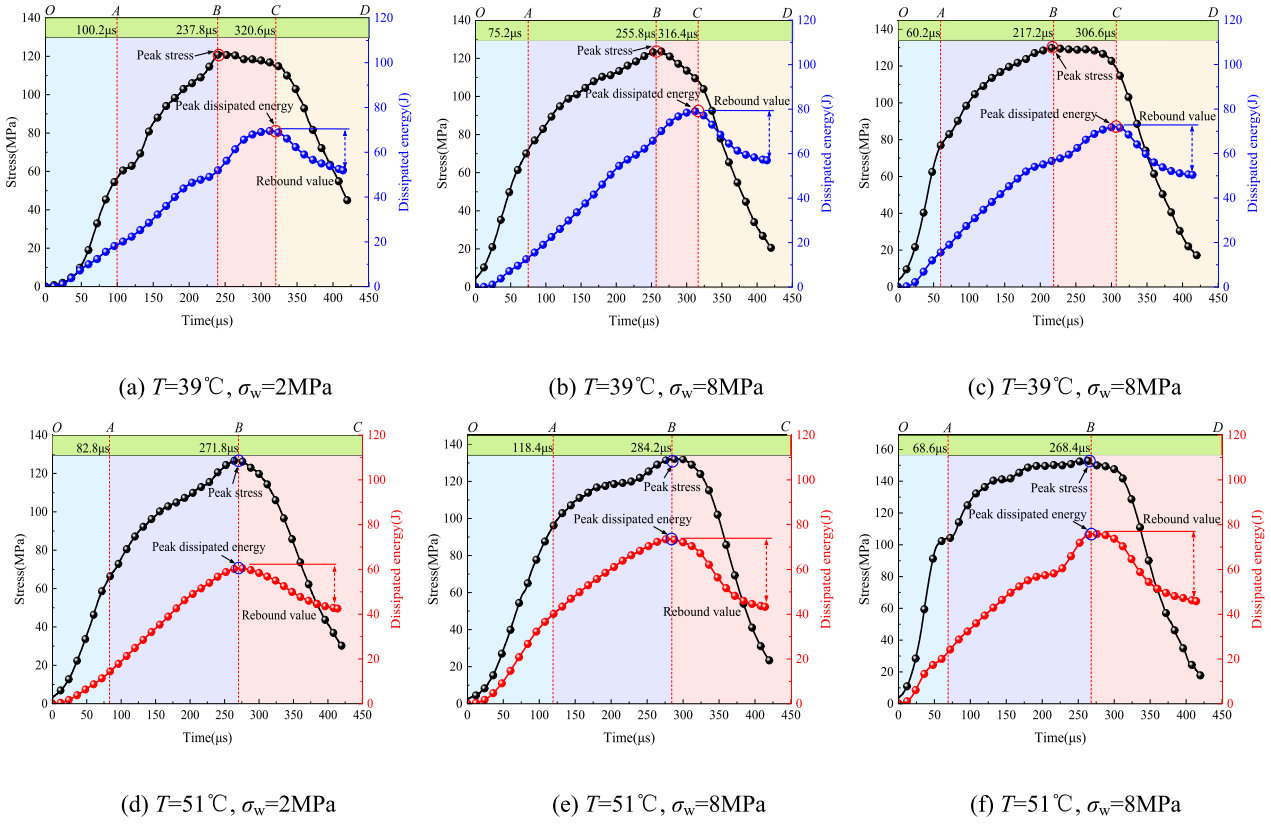

(a) T=39℃, σ_w=2MPa (b) T=39℃, σ_w=8MPa (c) T=39℃, σ_w=8MPa

(d) T=51℃, σ_w=2MPa (e) T=51℃, σ_w=8MPa (f) T=51℃, σ_w=8MPa

Fig.11. Stress-dissipated energy time history curve.

energy to maintain its load-bearing capacity, leading to its temporary storage of energy by means of elastic energy. This energy is subsequently released in the form of reflected stress waves and transmitted stress waves[44].

(2) Figs. 11a ~ c displays the stress-dissipated energy time evolution curves of rocks under various water pressures at T = 39℃. The four stages of the dynamic impact test procedure for deep rocks under THM coupling conditions are as follows:

OA stage (linear elastic stage): Point A represents the point of sudden change in the slope of the dynamic stress-time curve, i.e., the yield point. In OA stage, the dynamic stress rises linearly with time under the action of impact loads, and the original fractures within the rock fail to close under the impact loads, resulting in faster stress growth. The energy dissipated by fragmentation increases slowly and linearly with the propagation of stress waves.

AB stage (crack stabilization and propagation stage): Point B is the peak point of dynamic stress. During this stage, the dynamic elastic modulus dramatically drops, and the dynamic stress-time curve's slope steadily drops to zero, suggesting that rock cracks are still forming and spreading under the influence of high disturbance loads. After reaching the stress peak at point B, macro-cracks continue to appear; the energy dissipated by fragmentation continues to accumulate, showing a linear upward trend.

BC stage (crack acceleration stage): Point C is the peak point of fracture dissipation energy. In this stage, The dynamic stress-time curve has a negative slope. Under the rapid increase in fracture dissipation energy, macro-scale failure surfaces appear in the rock, cracks keep growing and spreading, and their carrying ability progressively diminishes. However, due to the energy lag phenomenon, the crack propagation velocity has a threshold and reaches its limit before the energy transfer velocity.

CD Stage (Destruction Stage): Point D represents the residual dynamic stress point. During this stage, stress decreases sharply, the slope of the dynamic stress-time curve drops abruptly, moreover, the energy dissipated through fragmentation decreases gradually. Ultimately, the energy is released through the fragmentation of rock blocks, destroying the rock. As water pressure rises, the rebound value of fracturing dissipation energy gradually increases, indicating that the applied water pressure acts as confining pressure, restricting radial deformation and preventing further development of internal fractures. This enhances the rock's load-bearing capacity to resist deformation, reducing the extent of rock failure. At this point, an increased rebound phenomena in dissipation energy results from an increase in the elastic energy stored in the rock.

Figs. 11d ~ f displays the stress-dissipated energy time evolution curves under various water pressures at T = 51℃. With increasing temperature, the dynamic impact test process of deep rock under THM coupling conditions only includes three stages: the OA stage (linear elastic stage), AB stage (crack stable propagation stage), and BC stage (failure stage). The rock dynamic stress and fracture dissipation energy simultaneously reach their peak values. Additionally, the rebound value of the fracture dissipation energy rises with the increase

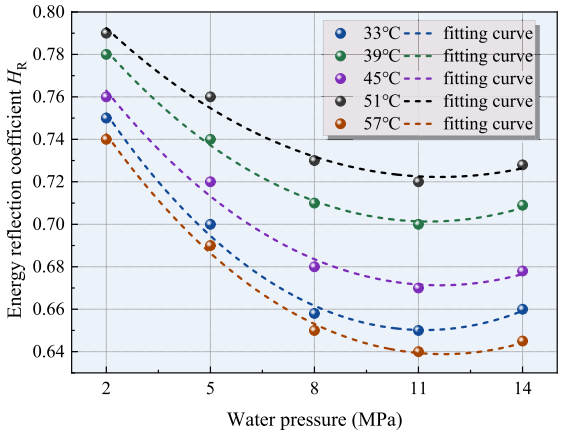

Fig.12. Changes in rock energy reflection coefficient under THM coupling.

T/℃	α	β	χ	R^2
33	0.191	0.023	1.01×10^{-3}	0.972
39	0.194	0.028	1.26×10^{-3}	0.998
45	0.212	0.032	1.38×10^{-3}	0.975
51	0.214	0.038	1.73×10^{-3}	0.986
57	0.229	0.037	1.59×10^{-3}	0.997

Table 2. Fitting results between rock energy reflection coefficient and water pressure.

in water pressure. The times for the increase in dynamic stress in Fig. 11a ~ c are 271.8 μs, 284.2 μs, and 268.4 μs, respectively, which are greater than those in Figs. 11d ~ f, which are 237.8 μs, 255.8 μs, and 217.2 μs, respectively. The primary reason lies in the thermal expansion forces brought on by temperature, which induce friction between mineral particles, leading to mutual compression between particles. The pressure within the pores causes the original internal pores and microcracks to close[45], resulting in a more compact internal structure of the rock and enhanced resistance to impact.

Energy reflection coefficient

Fig. 12 illustrates how the energy reflection coefficient of deep sandstone changes with water pressure at varying temperatures while maintaining the same impact force and axial pre-stress. As can be obtained from Fig. 12, with increasing water pressure, the energy reflection coefficient of deep rock first decreases rapidly and then develops gradually. For instance, when water pressure increases from 2 to 8 MPa, the rock energy reflection coefficient decreases sharply. However, when water pressure continues to increase beyond 8 MPa, the rock energy.

reflection coefficient tends to stabilise, with the overall range stabilising between 0.641 and 0.724 under different temperatures. To acquire more information about the variation law of rock energy reflection coefficients under different T-H conditions, the energy reflection coefficients and water pressure data in Fig. 12 were fitted, and it was found that the two satisfy an exponential function relationship

$$H_R = e^{(-\alpha-\beta\sigma_w+\chi\sigma_w^2)} \tag{7}$$

In the equation, α represents the constant value of the rock energy reflection coefficient under different temperature conditions, with a dimension of 1. Both β and χ characterise the rate of change of the rock energy reflection coefficient with water pressure, with a dimension of 1. The fitting curves of the rock energy reflection coefficient with water pressure under different temperature conditions are summarized in Fig. 12, and Table 3 lists the fitting parameter results.

The fit between the fitted curve and the experimental data in Fig. 12 and the fitted correlation coefficients in Table 2 displays that the function has a high correlation coefficient, and the rock energy reflection coefficient exhibits a good exponential relationship with water pressure. This fitted function model effectively characterises the relationship between water pressure and the rock energy reflection coefficient, providing a reference for stress wave energy reflection during dynamic disturbance excavation in underground water-rich engineering blasting operations.

Energy transfer coefficient

The energy transfer coefficient calculated based on transmitted waves can be more effectively used to invert changes in rock wave impedance and accurately characterise changes in rock physical and mechanical properties[44]. Fig. 13 displays the variation of the rock energy transfer coefficient under the same axial pre-

stress conditions and dynamic impact load. The rock energy transfer coefficient rises with increasing water pressure and exhibits an approximately linear upward trend under different temperature conditions. Under different water pressure conditions, the rock energy transfer coefficient first increases and then decreases with increasing temperature. Analysis suggests that when rock is subjected to a specific axial pre-stress, the degree of pore compaction or damage evolution is determined. An increase in water pressure has a dual effect on the rock's wave impedance, both enhancing and weakening it. The rise in water pressure favours an increase in the rock's water content, as pores previously filled with air or a vacuum are filled with free water. Since the density of water and its longitudinal wave velocity are greater than those of air, water pressure exerts a circumferential force on the rock, further increasing its density. Both of these effects contribute to an increase in the wave impedance, representing the enhancing effect of water pressure on the wave impedance. However, as water pressure continues to rise, the water content of the rock does not increase significantly; however, the water wedge effect formed by high water pressure promotes the propagation and breakthrough of microcracks in the rock, exacerbating the extent of rock damage and the softening effect of water on the rock, thereby reducing the rock's wave impedance value. This illustrates how water pressure reduces the impact of rock wave impedance.. At the same time, the increase in water pressure also enhances the circumferential force on the rock, causing the circumferential deformation of deep sandstone to be restricted under the same impact load, making the initiation and propagation of cracks increasingly difficult. The rock's energy transfer coefficient rises as a result of the majority of the impact energy traveling through it as stress waves. As the temperature gradually increases, the mineral particles inside the rock expand due to heating. The inconsistent thermal expansion and deformation of various mineral particles generate structural thermal stress, causing the original fractures to close. The initial damage to the rock gradually decreases, and its overall wave impedance increases, leading to an overall increase in the energy transfer coefficient. At this point, the enhancing effect of increased water pressure on the wave impedance significantly outweighs its weakening effect, and the transfer coefficient gradually tends toward linear increase. In summary, as water pressure gradually increases, its enhancing effect on rock wave impedance is greater than its weakening effect. As the temperature rises, the enhancing effect becomes increasingly dominant over the weakening effect, and wave impedance tends to increase linearly. However, as temperature continues to rise, the structural thermal stress produced within the rock becomes increasingly significant, and the enhancing effect of temperature on rock wave impedance begins to be outweighed by its weakening effect, resulting in a decrease in the energy transmission coefficient. This suggeststhat the proportion of transferred energy increases with decreasing rock dynamic damage extent. Sandstone is significantly harder than typical coal rock, which is advantageous for the transmission of stress wave energy. Based on wave impedance matching effects, if reflected energy is minimal and dissipated energy is maximised, rock fragmentation is more severe, and energy utilisation efficiency is higher. Therefore, under thermo-hydro-mechanical coupled effects, low-wave impedance explosives should be prioritised for deep engineering rock blasting to effectively enhance blasting energy utilisation efficiency.

Energy dissipation coefficient

Energy accumulation and dissipation cause deep rocks to become unstable and fail[46]. During dynamic loading, damage and plastic deformation of rocks cause energy dissipation. Energy dissipation deteriorates the dynamic properties of rocks, reducing the cohesion between particles and their resistance to failure. Therefore, dissipation of energy is a crucial characteristic of rock failure, reflecting the process of microcracks continuously forming, propagating, and connecting within the rock. The greater the energy dissipated during rock failure, the more energy the rock requires to dissipate during fracturing, which means that more microcracks must form during rock failure. Fig. 14 shows that the rock energy dissipation coefficient varies with water pressure under the same impact load and pre-stress but different temperature conditions. As can be seen from Fig. 14, water pressure has a crucial impact on the rock energy dissipation coefficient; as water pressure gradually rises, the rock energy dissipation coefficient first rises and then decreases; under different temperature conditions, the energy dissipation coefficient reaches its maximum value when water pressure is around 8 MPa. These results indicate

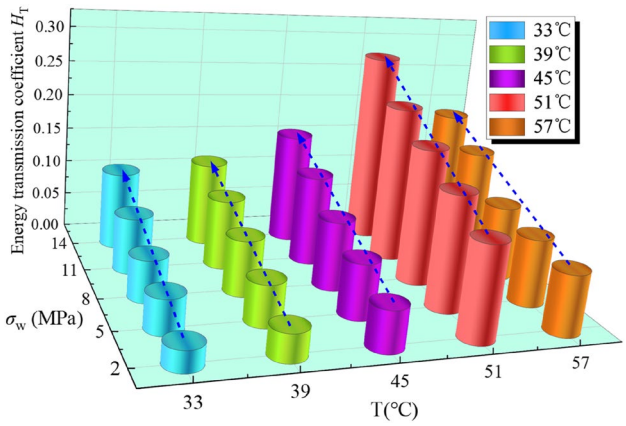

Fig.13. Variation trend of rock energy transfer coefficient under different temperature and water pressure.

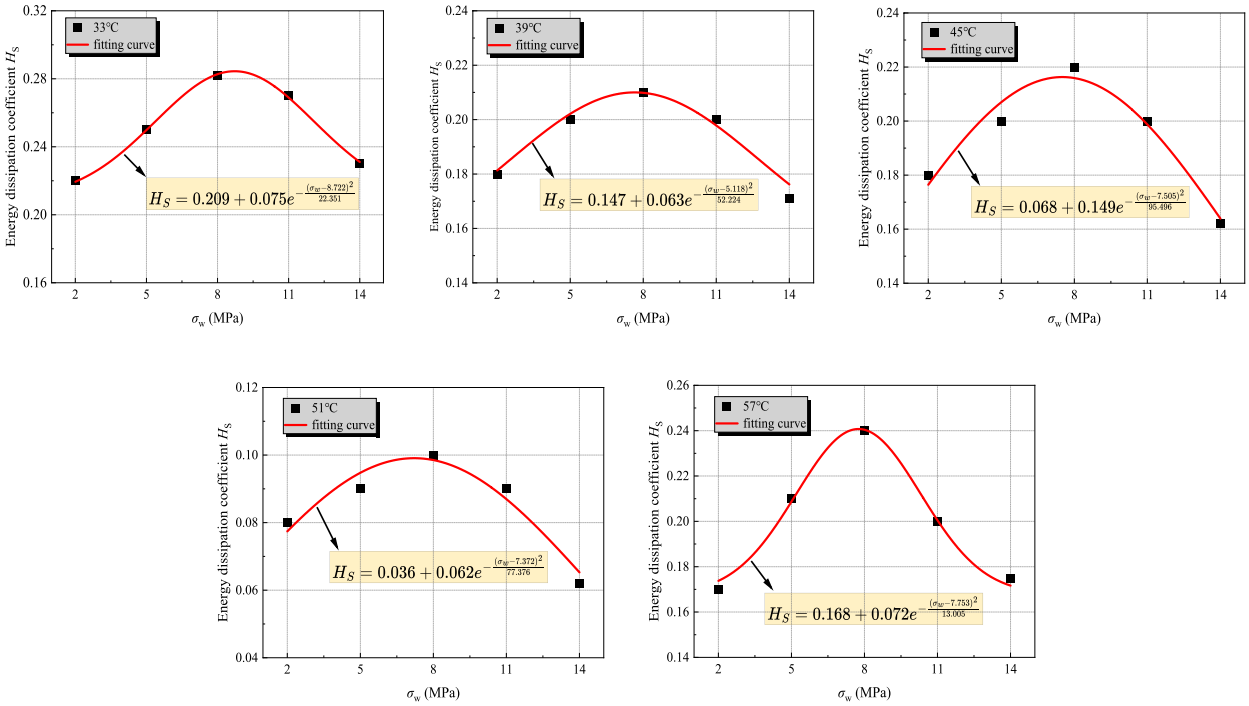

Fig.14. The change law of the energy dissipation coefficient.

that when water pressure increases to 8 MPa, the increase in water pressure promotes the absorption of rock energy; however, when water pressure continues to increase beyond 8 MPa, the increase in pressure inhibits the absorption of rock energy. According to the analysis, there are two distinct ways that water pressure affects the rock energy dissipation coefficient. The rise in water pressure promotes a rise in the water content within the rock. Under the action of impact loads, the expansion of existing fractures and the formation of new micro-fractures require more energy to overcome the viscous effects of water, leading to an increase in the rock's energy dissipation coefficient. As water pressure increases, the circumferential forces acting on the rock also increase. Under the same impact load, the rock's skeletal structure becomes more resistant to deformation, making it harder to fracture, which reduces the rock's energy dissipation coefficient, moreover, which initially increases due to the rapid increase in free water content within the rock as water pressure rises, leading to an increase in the energy required to overcome the viscous effects of water. At this stage, the rock's water content holds a dominant role in increasing energy dissipation, thereby increasing the energy dissipation rate of the sandstone. When water pressure continues to increase beyond 8 MPa, the free water content within the rock does not undergo significant changes, and the enhancing effect of water content on energy dissipation gradually weakens; however, the circumferential water pressure acting on the rock enhances its skeletal resistance to deformation. At this point, the reducing effect of circumferential water pressure on energy dissipation becomes dominant, causing the rock's energy dissipation rate to continue decreasing.

Additionally, when the temperature rises from 31 °C to 51 °C, the energy dissipation coefficient shows an overall decreasing trend. The rock requires less energy to dissipate during the dynamic fracture process, resulting in fewer microcracks during failure and an overall reduction in the severity of failure. This indicates that temperature plays an inhibitory role in internal damage to the rock during this process. When the temperature continues to rise to 57 °C, the energy dissipation coefficient begins to increase gradually. The rock requires more energy to dissipate during dynamic fracturing, resulting in the formation of more microcracks during failure and an overall increase in the severity of damage. This suggests that temperature plays a promoting role in internal injury to the rock during this stage.

In conclusion, the dual impacts of increased and diminished energy absorption by the rock during the rise in water pressure are responsible for the variable pattern of the energy dissipation coefficient illustrated in Fig. 14. The slope of the variation curve represents the difference between these dual effects; When the slope is positive, the enhancing effect dominates, and rised water pressure promotes rock energy absorption; when the slope is negative, the weakening effect dominates, and increased water pressure inhibits rock energy absorption.

To obtain more information on the variation of the water pressure with energy dissipation coefficient, the energy dissipation coefficient and water pressure in Fig. 14 were fitted. Table 3 displays that the fitting equation and fitting parameters.

In the table,κ represents the minimum energy dissipation coefficient of rock, γ represents the critical water pressure, with units in MPa. When σ_w is less than γ, the rock energy dissipation coefficient rises with increasing water pressure; When σ_w exceeds γ, the rock energy dissipation coefficient decreases with rising water pressure. Considering the characteristics of the Gaussian function,a larger parameter δ indicates a broader range of water pressures influencing the energy dissipation rate. Therefore,δ represents the sensitive water pressure range, with

Temperature	Gaussian function $H_S = \kappa$ equation($+ \psi \exp\left(-\frac{(\sigma_w - \gamma)^2}{2\delta^2}\right)$)				R^2
	κ	ψ	γ	δ	
33℃	0.209	0.075	8.722	22.351	0.991
39℃	0.147	0.063	5.118	52.224	0.985
45℃	0.068	0.149	7.705	95.496	0.957
51℃	0.036	0.062	7.372	77.376	0.937
57℃	0.168	0.072	7.753	13.005	0.966

Table 3. Fitting results between rock energy dissipation coefficient and water pressure.

units in MPa. Additionally, according to the fit between the fitted curve and experimental data in Fig. 14 and the correlation coefficients in Table 4, which displays that the rock energy dissipation coefficient exhibits a good Gaussian function distribution with respect to water pressure.

Macro-dynamic damage characteristics

Destruction mode

Analyzing the failure patterns of rocks subjected to strong disturbances can provide the most direct criteria for safe excavation and stable support of surrounding rock in deep coal[47]. Typical failure patterns of rocks under different temperature conditions and water pressure are listed in Table 4. Under the coupled effects of temperature, water pressure, and stress, the lateral cracks in rocks are mainly shear cracks. As water pressure gradually increases, the development scale (number, length, and width) and failure severity of lateral shear cracks in rock decrease. This is because, as water pressure rises, the viscous effects generated by free water within the rock gradually strengthen, and water pressure can restrict lateral deformation of the rock, thereby inhibiting the initiation and propagation of microcracks. As shown in the table, under the same temperature conditions (33 °C), when water pressure is low, rock damage is most pronounced, with irregular polygonal fracture surfaces and relatively large.

fragment sizes. When water infiltrates the rock, soluble salts dissolve and colloidal minerals hydrolyze, transforming the original bonds into hydrogel bonds. The bonding strength between mineral particles weakens, friction decreases, and water in the surrounding environment produces a lubricating effect on discontinuous surfaces. The shear stress effect on discontinuous surfaces is enhanced, leading to the fragmentation of rock pieces along shear cracks, with shear edges exposed. The ultimate failure mode of the rock is compression-shear crushing failure. When water pressure is high, shear cracks are only distributed in the rock boundary area, and the degree of dynamic impact damage is reduced. One-quarter of the rock is broken, while three-quarters remain relatively intact. The damaged fragments are mostly from the sample boundary area, with the fragments being thin and elongated.

The rock failure mode is inclined shear boundary failure, corresponding to the flaking phenomenon of the deep surrounding rock. Under the same water pressure conditions (8 MPa), as the temperature increases, the rock mass remains intact, with only shear cracks forming at a certain angle to the impact stress on the sides. Ultimately, no failure occurs, and the rock failure mode is fracture failure. Analysis suggests that rising temperatures cause thermal expansion of mineral particles within the rock, leading to deformation and the generation of structural.

SC represents a shear crack.

thermal stress. When thermal stress and water pressure are coupled, the interlocking forces between different mineral grains strengthen, causing their original microcracks to close. Additionally, free water within the rock inhibits the further development of microfractures triggered by structural thermal stress, causing the total amount of rock failure to diminish as well as the quantity of microcracks.

Damage variable

To characterize changes in the extent of dynamic damage to deep rock under THM coupling, the P-wave velocity of specimens that did not undergo overall fragmentation after impact was measured using a seismic velocity meter. Relative velocity and damage degree were used as evaluation parameters to assess the extent of internal damage to deep rock after impact under THM coupling:

$$V_T = \frac{V_m}{V_0} D = 1 - \left(\frac{V_m}{V_0}\right)^2 \tag{8}$$

where,D represents the damage variable, V_T represents the relative wave velocity, V_m reprensents the P-wave velocity of the rock that has not undergone compressive shear crushing failure after the impact, and V_0 represents the P-wave velocity of the rock before the impact.

The longitudinal wave velocity, relative wave velocity, and damage degree of rock without compression-shear crushing failure after impact under THM coupling are displayed in Table 6. Under the impact of THM coupling,

Water stress σ_w/MPa	Temperature T/℃	Dynamic strength σ_c/MPa	Incident energy Q_I/J	Strain rate $\dot{\varepsilon}$/s^{-1}	Failure pattern	Final images of rock specimen
2	33	117.11	261.14	123.1	compression-shear crushing failure	
5	33	122.22	253.56	124.1	compression-shear crushing failure	
8	33	124.92	260.18	129.4	compression-shear crushing failure	
11	33	126.52	265.71	132.5	inclined shear boundary failure	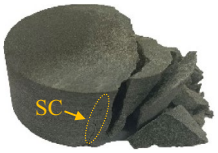
14	33	127.15	274.92	142.8	inclined shear boundary failure	
8	39	125.18	276.62	131.2	inclined shear boundary failure	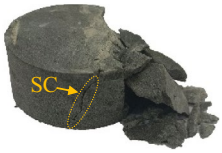
8	45	128.33	286.62	146.2	fracture failure	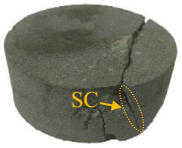
8	51	139.41	265.71	158.4	fracture failure	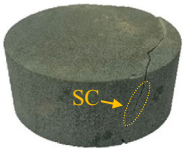
8	57	130.68	272.89	152.9	fracture failure	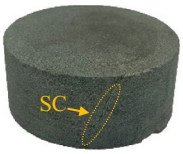

Table 4. Typical rock failure modes under different water pressures and temperatures.

the rock under some working conditions has undergone compression-shear crushing failure, and its longitudinal wave velocity cannot be measured, so it is not listed in the table. According to the test data in Table 5, the damage.

variable D and the relative wave velocity V_T of the rock after the impact load change with the water pressure, as displayed in Fig. 15. The deep rock without compression-shear crushing failure after impact under THM coupling, the relative wave velocity increases with the rise of water pressure, while the rock damage variable is smaller and the decreasing trend is gradually gentle. Under the same water pressure condition, the greater the overall temperature, the smaller the damage degree of the rock after the impact. Combined with the previous analysis, the increase in water pressure has both strengthening and weakening effects on the resistance of rock to deformation under impact. The enhancement effect reduces the damage degree of rock after impact, and the

Water stress σ_w/MPa	Temperature T/℃	Saturated longitudinal wave velocity V_0/(m/s)	Longitudinal wave velocity after impact V_m/(m/s)	relative wave velocity D	
11	33	2866	2201	0.763	0.417
14	33	2933	2323	0.787	0.380
8	39	2941	2212	0.748	0.441
11	39	2944	2274	0.768	0.410
14	39	2987	2379	0.792	0.373
2	45	2924	2255	0.767	0.412
5	45	2704	2122	0.780	0.391
8	45	2712	2149	0.788	0.380
11	45	3220	2573	0.795	0.369
14	45	2902	2306	0.790	0.376
2	51	2895	2272	0.780	0.391
5	51	2934	2366	0.802	0.357
8	51	2715	2233	0.818	0.332
11	51	2801	2273	0.807	0.349
14	51	3169	2615	0.820	0.327
2	57	2955	2284	0.768	0.410
5	57	2949	2338	0.788	0.379
8	57	2923	2355	0.801	0.358
11	57	2916	2379	0.811	0.342
14	57	2895	2346	0.806	0.351

Table 5. P-wave velocity, relative wave velocity and damage degree without compression-shear crushing failure after impact.

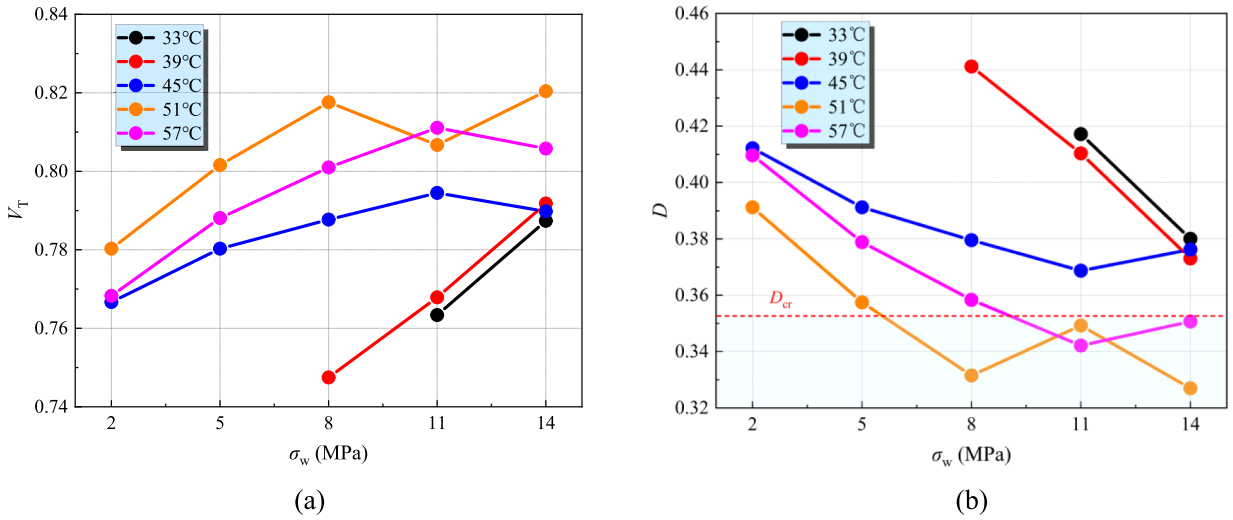

Fig.15. The influence of σ_w on relative wave velocity and damage variable.

weakening effect leads to the gradual decrease of damage variable. Additionally, combined with the evolution law of rock energy dissipation coefficient with water pressure, it can be seen that it is consistent with the evolution law of damage variable of rock without compression-shear crushing failure after impact, which can be proved by each other. In addition, combined with the statistical rock damage variable and the actual damage degree, the damage threshold D_{cr} corresponding to the rock under THM coupling and impact load can be delineated between 0.35 and 0.36, that is, the imaginary line position in the graph. When the damage variable D is less than the damage threshold D_{cr}, there are only tiny cracks on the rock surface, and no fragments are falling off, and the rock integrity is better. The majority of working situations in engineering practice allow for the monitoring or control of the water pressure and temperature range. According to the size of water pressure and temperature, the macroscopic damage degree and range of rock mass are determined, and the ultrasonic test is used to verify the feedback. It can provide a reference for engineering construction design.

Meso-microscopic structures

Meso-structure

A detailed examination of the fracture process reveals the complex evolution of primary fractures along weak structural planes in rock masses under the effect of stress waves. To further analyze the dynamic failure mechanisms under the combined effects of "three highs and one disturbance," a Bystronic electronic digital microscope magnified 1000 times was used to examine typical failure surfaces of rock masses subjected to temperatures of $T = 45$ °C and stress levels of $\sigma_w = 5$ MPa, 11 MPa, and 14 MPa, as presented in Fig. 16. Some areas of the rock failure surface still have structurally weak surfaces formed by primary joint layers and cavities. Under external loads, these structurally weak surfaces undergo complex evolution, with mineral particles peeling away from each other, forming a great amount of new cracks and nurturing them. The cracks interconnect with each other, ultimately causing the rock to fail along the structurally weak surfaces. Figure 16a shows the microstructure at the rock failure surface when $\sigma_w = 5$ MPa. At this point, fracture propagation is primarily driven by stress waves, causing the mineral grains within the rock to transition from a state of equilibrium to a state under stress. This leads to the nucleation, propagation, and formation of numerous new fractures, joints, and faults at the original defects within the rock structure (such as bedding planes, joints, and primary fractures). Figs. 16b and c

show the microstructures at the rock failure surface when $\sigma_w = 11$ MPa and 14 MPa, respectively. It can be obtained that as σ_w rises, the width of fractures, joints, and faults at the rock failure surface decreases, and the extent of internal damage to the rock gradually decreases. This indicates that increased water pressure can promote the closure of natural fissures, hinder the formation and expansion of new fractures, and, on a macroscopic scale, prevent rock debris from flying, thereby constraining lateral deformation of the rock. Thus,

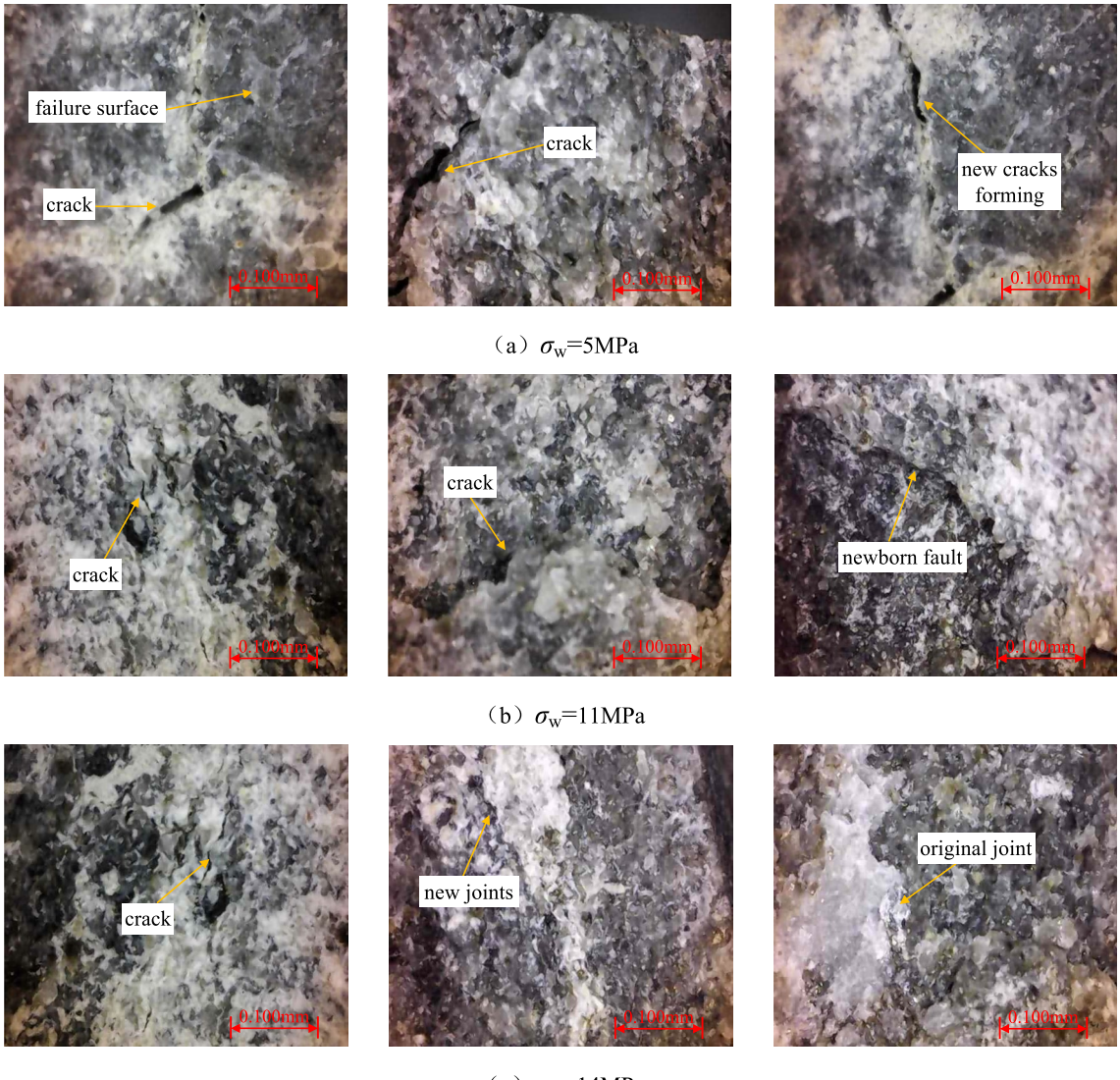

Fig.16. Microscopic structure at the rock failure surface.

water pressure has a certain strengthening mechanism on the weak surfaces of the internal structure of rock under specific multi-field coupling conditions.

Microstructure test

SEM can observe the local microstructure of deep rock cross-sections, thereby revealing the patterns of change in the internal pore and fracture structures of rocks. Using SEM to scan the microstructure of rock fracture surfaces after exposure to a temperature of 33 °C and different water pressures, as depicted in Fig. 17. After undergoing thermal-hydro-mechanical coupled effects, the internal fracture surfaces of the rocks are covered with a large amount of rock debris. The fracture surfaces are overall rough and uneven, with poor uniformity. The rock debris attachments are primarily fine-grained minerals, with loose intergranular cementation and widespread development of microcracks. Rock itself is composed of mineral particles of various sizes and types that are cemented together. The infiltration of water causes the hydrophilic minerals and cementing agents within the rock to undergo physical and chemical dissolution reactions. In this process, hydrophilic mineral particles undergo ion.

exchange with water, thereby weakening the bonding between mineral particles and ultimately resulting in the formation of more fractures within the rock. As seen in Fig. 17a and b, when water pressure is low, there are more cracks between mineral particles within the rock, resulting in a looser particle structure and a rough surface texture. As water pressure increases, as depicted in Fig. 17c ~ e, the number of fractures within the rock gradually decreases. The increased external water pressure causes the micro-pores between mineral particles to close, while the small fractures interconnect to form elongated cracks, resulting in a smooth surface texture. As can be obtained from Fig. 17, when σ_w is 2 MPa and 5 MPa, the structure between mineral particles gradually becomes loose, with some particles directly detaching from the cross-section. The surface becomes uneven, with irregular edges and corners appearing. The fracture surface exhibits a large amount of intact crystal particles, and intergranular fractures occur in the weakly bonded cemented phases. The primary form of fracture within the rock.

is intergranular fracture. Analysis of causes: The primary stress acting on the rock stems from axial impact disturbances and pre-existing stress. These unidirectional mechanical effects cause mineral particles to preferentially choose easier failure paths[48], i.e., failure of the cementing phase between mineral particles, resulting in intergranular fracture. When σ_w is 8 MPa and 11 MPa, the fracture surface simultaneously exhibits separated crystal particles and open cracks penetrating the particle surfaces, combining both intergranular and transgranular fracture characteristics, constituting a composite fracture. When σ_w increases to 14 MPa, the edges of the rock's internal fracture surface become sharp and distinct, with a more compact internal structure. Adjacent mineral particles have flush fracture surfaces, primarily characterized by face-to-face contact. Microfractures

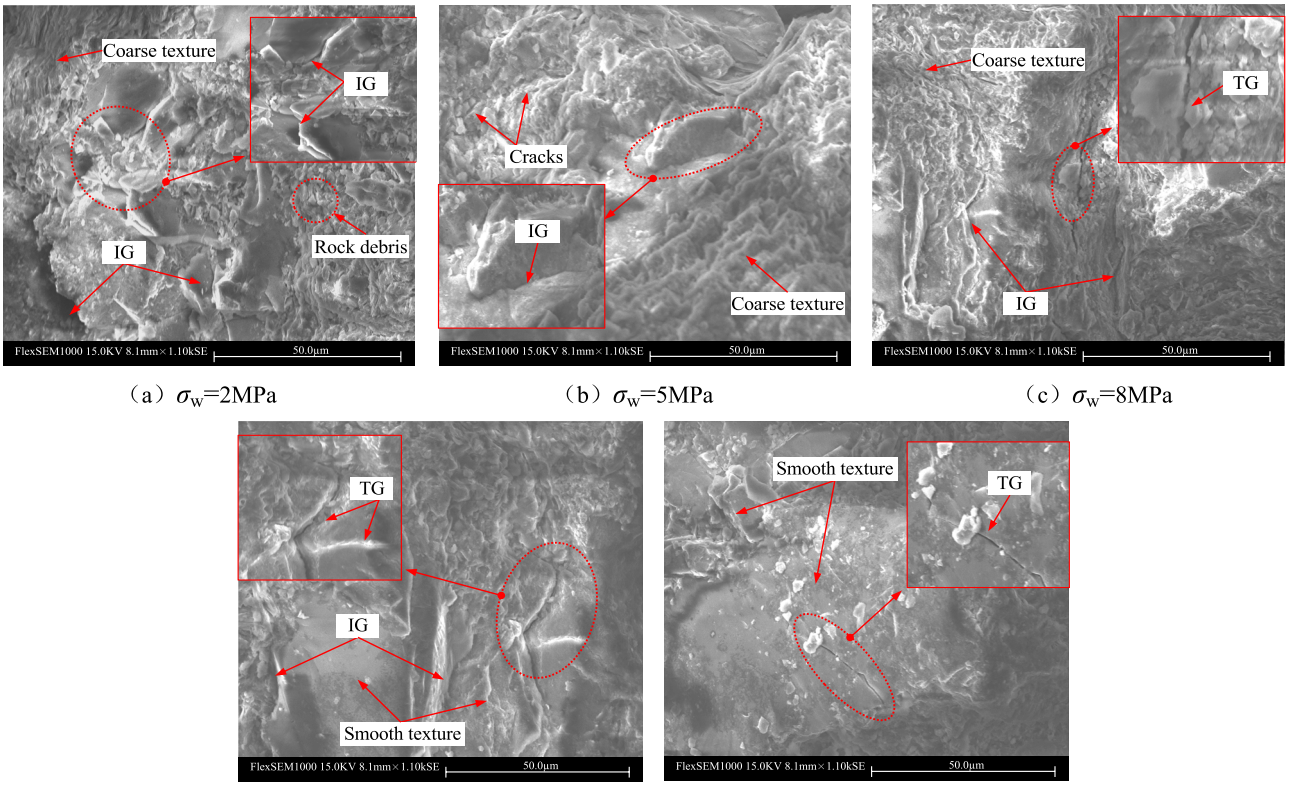

（a）σ_w=2MPa　（b）σ_w=5MPa　（c）σ_w=8MPa

（d）σ_w=11MPa　（e）σ_w=15MPa

Fig.17. Microstructural morphology of rock fractures under different water pressures (T=33℃).

run straight through the entire particle, with intergranular fracture occurring directly within the crystal grains, exhibiting strong shear fracture characteristics. At this point, the primary fracture form within the rock's internal fracture surface is intergranular fracture. On account of the rise in water pressure, the lateral stress state of the rock becomes more pronounced, while the development time of microfractures is extremely short. Under the coupled effects of thermal, hydrothermal, and mechanical forces, most mineral grains do not have sufficient time to select weaker failure paths, making intergranular fracture more likely to occur.

Pore structure characteristics

Nuclear magnetic resonance (NMR) technology can accurately determine the porosity, permeability, and pore size distribution of rocks. NMR testing yields the T_2 relaxation time spectra of rocks at $T = 51$℃ under different water pressures, as illustrated in Fig. 18. A leftward shift in the T_2 spectrum curve indicates a decrease in the pore size within rock interiors, while an upward rise in the T_2 spectrum curve indicates an rise in the number of pores with identical aperture[49]. It can be obtained that under THM coupling, the T_2 distribution curve of the rock exhibits a bimodal shape (main peak and secondary peak), with the amplitude of the main peak being significantly higher than that of the secondary peak. Under the same temperature conditions, the amplitudes and areas corresponding to the secondary peak and main peak decrease with increasing water pressure. For rock samples subjected to a temperature of $T = 51$℃, the main peak area and secondary peak area at $\sigma_w = 2$ MPa are 12,304 and 559, respectively. At $\sigma_w = 5$ MPa, 8 MPa, 11 MPa, and 14 MPa, the main peak areas decrease to 11,522, 10,432, 9,708, and 9,131, respectively, with decreases of 6.4%, 15.1%, 21.1%, and 25.8%. The secondary peak areas at $\sigma_w = 5$ MPa, 8 MPa, 11 MPa, and 14 MPa were 512, 497, 463, and 444, respectively, representing reductions of 8.4%, 11.1%, 17.2%, and 20.6% compared to the secondary peak area at $\sigma_w = 2$ MPa. Additionally, as water pressure increases, both the main peak and secondary peak exhibit a trend toward leftward shift, reflecting the process of pore enhancement in rock samples under water pressure. For instance, when water pressure rises from 2 to 14 MPa, the T_2 spectral values corresponding to the main peak of the rock are 0.61 ms, 0.52 ms, 0.43 ms, 0.42 ms, and 0.41 ms, respectively. Among these, the T_2 spectrum values of the main peak under water pressures of $\sigma_w = 5$ MPa, 8 MPa, 11 MPa, and 14 MPa decreased by 14.7%, 29.5%, 31.1%, and 32.8%, respectively, compared to those under $\sigma_w = 2$ MPa.

Fig. 19 shows the distribution of amplitude values corresponding to the main peak and secondary peak of rock under different water pressures. When the temperature remains constant, as water pressure rises, the amplitudes corresponding to the main peak and secondary peak in the rock T_2 spectrum curve gradually decrease. At $\sigma_w = 2$ MPa, the amplitude corresponding to the main peak is 444.37, and at $\sigma_w = 5$ MPa, 8 MPa, 11 MPa, and 14 MPa, the corresponding amplitudes decrease to 377.71, 347.78, 338.61, and 287.82, respectively, with decreases of 15%, 21.7%, 23.8%, and 35.2%; at $\sigma_w = 14$ MPa, the amplitude corresponding to the secondary peak is 35.27, while at $\sigma_w = 2$ MPa, 5 MPa, 8 MPa, and 11 MPa, the amplitudes corresponding to the secondary peak are 42.35, 41.97, 40.06, and 38.91, respectively, representing increases of 20%, 19%, 13.6%, and 10.3% compared to the amplitude corresponding to the secondary peak at $\sigma_w = 14$ MPa. These data provide a more intuitive understanding of the evolution of pore structure in rocks under multi-field coupling and impact loads. Changes in pore structure affect the physical and mechanical properties of rocks. Analyzing changes in the pore structure of deep rocks under different water pressures can offer a theoretical basis for rock engineering design and stability assessment, helping to optimize solutions and reduce risks.

Studies on rock nuclear magnetic resonance testing have confirmed that T_2 has the property of reflecting the pore size distribution and size within the rock. In rock pore fluids, there are Three types of relaxation mechanisms: surface, diffusion, and volume relaxation. Among these, surface relaxation and volume relaxation affect both T_1 and T_2, while diffusion relaxation under a magnetic gradient field only affects the transverse relaxation time T_2. The three relaxation effects influencing T_2 are given by Eq. (14):

$$\frac{1}{T_2} = \frac{1}{T_{2B}} + \frac{1}{T_{2S}} + \frac{1}{T_{2D}} \tag{9}$$

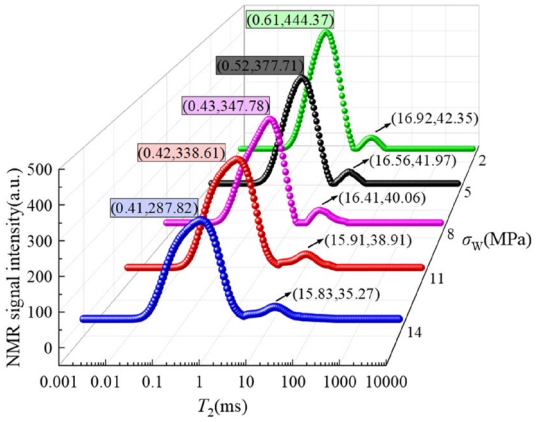

Fig.18. T_2 spectrum curves under different water pressures.

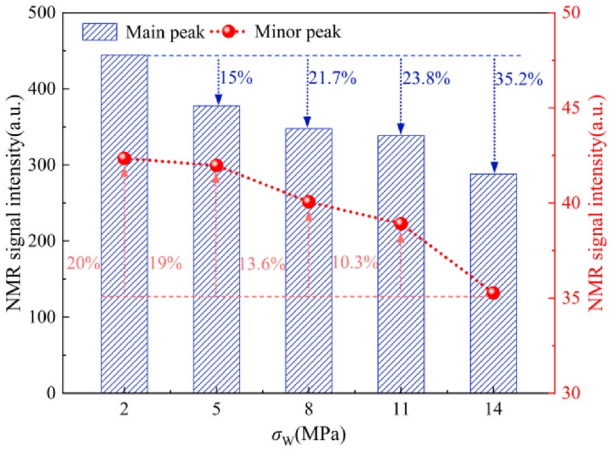

Fig.19. Amplitude sizes corresponding to the main peak and secondary peak of rocks under different water pressures.

In the equation, T_2 represents the transverse relaxation time of nuclear magnetic resonance, ms;T_{2B} represents the transverse volume relaxation time in the core fluid, ms;T_{2S} represents the transverse surface relaxation time, ms;T_{2D} represents the diffusion relaxation time of pore fluid in gradient nuclear magnetic resonance, ms.

In Eq. (14), T_{2B} is determined by the fluid in the pores, and T_{2S} represents a relationship related to the pore size. During the experiment, since the rock was completely immersed and saturated with water, the volume relaxation rate of water T_{2B} was extremely large, and $1/T_{2B}$ could be neglected. In this case, $1/T_{2D}$ was also very small, and the bond T_2 with the pore size could be approximately simplified to[50]:

$$\frac{1}{T_2} \approx \frac{1}{T_{2S}} = \rho_2 \left(\frac{S}{V}\right)_{pore} \tag{10}$$

In the equation, ρ_2 represents the surface relaxation rate; S and V represent the surface area and fluid volume of the pores, respectively. Therefore, the distribution of the T_2 spectrum can reflect the pore size distribution characteristics of the rock. The pore structure of sandstone is intricate and varies greatly in size. Research has found that the difference between large and small pore sizes can be as much as five orders of magnitude, resulting in different compressibility of pores of different sizes when subjected to external forces. Currently, based on capillary cohesion theory, scholars at home and abroad have proposed some pore size classification methods, but there is no unified standard for accurately classifying sandstone pore sizes. The sandstone pore size classification method proposed by Song[51] was adopted to classify pore sizes into three scale ranges: microporous($r_c \leq 0.1$ μm), mesoporous(0.1 μm $< r_c \leq 1$ μm), and macropores($r_c > 1$ μm). The schematic diagram of rock pore size classification is summaried in Fig. 20a.

Figs. 20b ~ f displays the pore size distribution features of rock pores under various water pressures. The water pressure has a promoting effect on the pore size distribution of deep rock samples. As water pressure increases, the porosity of pores of different diameters decreases significantly, and the total porosity decreases with increasing water pressure. Under the same temperature conditions, the pore size distribution characteristics of rock samples under different water pressures remain largely consistent, primarily consisting of micro-pores, with a relatively small proportion of mesopores and macro-pores. Additionally, comparative data under different water pressures dispaly that the proportion of porosity in each pore size distribution range decreases as water pressure increases. According to the above results, the analysis shows that the mechanical mechanism behind this phenomenon arises from the application of water pressure, which is similar to the confining pressure effect. Confining pressure constrains the pore structure of rocks, and high confining pressure hinders the stress wave propagation, limiting rock deformation and changes in pore structure. To a certain extent, it exerts a compaction effect on the micro-pores of rocks, with the restrictive effect becoming stronger as water pressure increases. Additionally, thermal expansion forces caused by temperature and pre-existing stress within a certain range also contribute to the closure of existing fractures, preventing further development of internal fractures in the rock. This enhances the rock's ability to resist deformation. Therefore, as water pressure increases, the pore diameters within the rock gradually decrease, and the total porosity gradually decreases. The mechanical characteristics of rock are directly impacted by changes in the distribution of pore sizes, such as strength and toughness. By analyzing changes in pore size distribution, we can provide a microscopic explanation and prediction of the mechanical characteristics of rock in engineering applications. For example, in engineering projects such as tunnel excavation and mine blasting, understanding the rock's dynamic mechanical properties changes after THM coupling and impact can help us design reasonable construction plans and ensure engineering safety.

Discussion

Sandstone is a typical aggregate polycrystalline material with numerous micro-pores and micro-cracks within its structure. Under THM coupling conditions, Because of thermal expansion anisotropy within a single

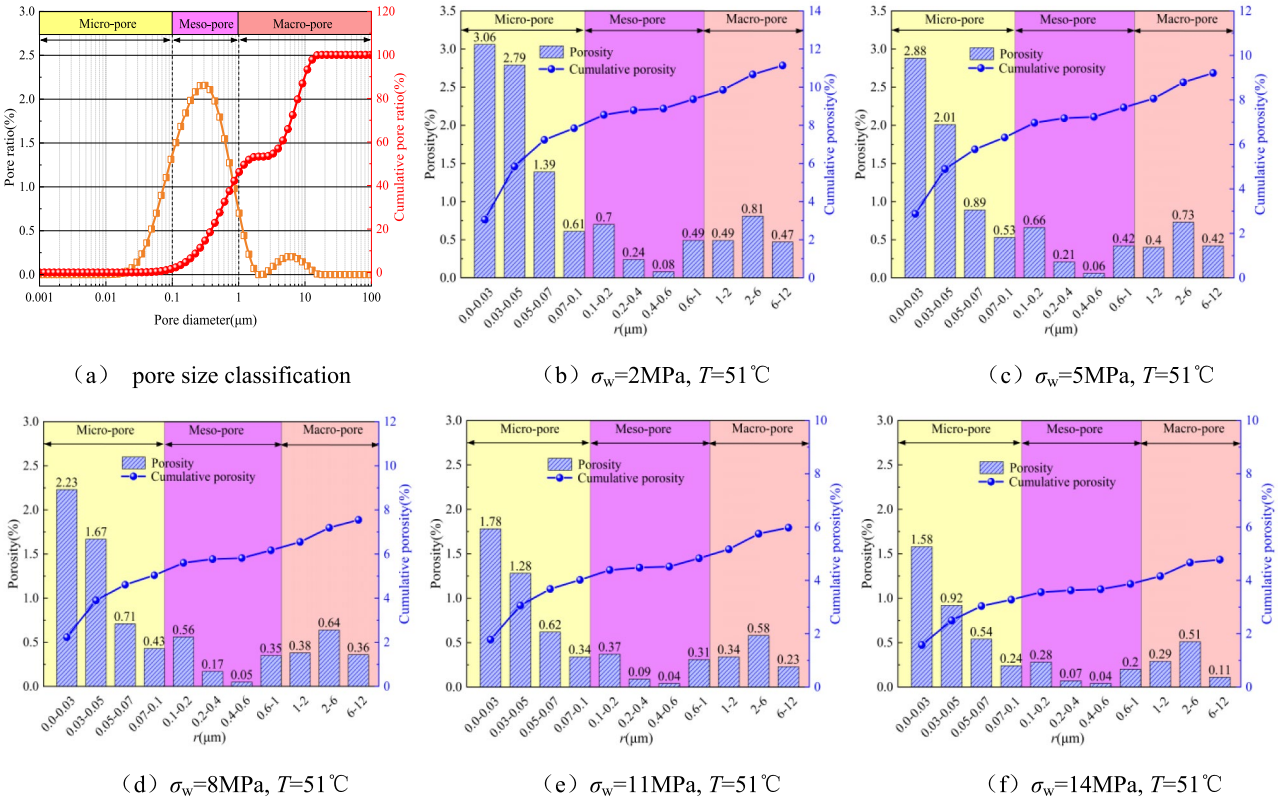

（a） pore size classification

（b） σ_w=2MPa, T=51℃

（c） σ_w=5MPa, T=51℃

（d） σ_w=8MPa, T=51℃

（e） σ_w=11MPa, T=51℃

（f） σ_w=14MPa, T=51℃

Fig.20. Pore characteristics inside rocks under different water pressures.

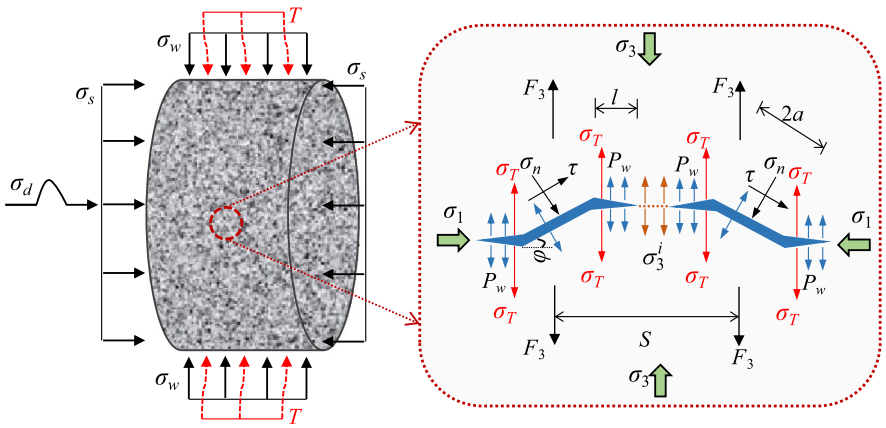

Fig.21. Schematic diagram of slip crack propagation model under THM coupling.

mineral particle and thermal expansion mismatches between distinct mineral particles, the rock may develop intergranular and intragranular micro-cracks. Moreover, under the influence of pore water pressure and shear stress, existing micro-cracks may also propagate and extend. Therefore, based on the Ashby-Sammis microscopic mechanical model[53], a THM-coupled and impact load-induced microcrack propagation model is established to reflect the dynamic mechanical feature of brittle rocks. This model aims to investigate the effect mechanism of THM coupling conditions on microcrack propagation pathways during the dynamic failure process of deep rocks, thereby providing an intuitive understanding of the internal damage evolution patterns and dynamic failure mechanisms of rocks. Fig. 21 displays a schematic diagram of the rock internal slip-type crack propagation model under THM coupling and impact loading. Water pressure, axial static stress, and uniform impact stress are applied to the rock's far-field boundary. The microcrack surface encounters pore water pressure, and the crack tip experiences thermal expansion stress as a result of the rock's complete saturation and the mineral particles' thermal expansion. It is assumed that the sum of the axial static stress σ_s and the impact stress σ_d

equals the maximum principal stress σ_1, and the water pressure σ_w equals the second principal stress and the minimum principal stress σ_3, i.e.:

$$\sigma_1 = \sigma_s + \sigma_d \tag{11}$$

$$\sigma_2 = \sigma_3 = \sigma_w \tag{12}$$

Microcracks include initial cracks and wing cracks at an angle of σ_1 to ϕ degrees with respect to the direction of the maximum principal stress, with lengths of $2a$ and , respectively. According to previous research[Error! Reference source not found.], the following is a simplified version of the wing fracture propagation path: under the influence of the stress intensity factor, the crack first propagates at a large angle along the direction of compressive stress, and ultimately fractures quickly follow the path of compressive stress. Meanwhile, shear stress τ and normal stress σ_n are generated by the far-field stress during the initial crack slip. Under THM coupling conditions, these stresses can be calculated using Eqs. (13) and (14) based on the coordinate transformation of stress components.

$$\sigma_n = \frac{(\sigma_1 + \sigma_3) - (\sigma_1 - \sigma_3)\cos 2\phi}{2} + \lambda P_w \tag{13}$$

$$\tau = \frac{(\sigma_1 - \sigma_3)\sin 2\phi}{2} \tag{14}$$

In the equation, P_w represents pore water pressure, and λ represents the water wedge coefficient, which is related to the water wedge effect within the rock. Due to the rapid disturbance and impact loads on the rock, the water contained in the internal microcracks cannot be expelled in time, so it can be considered that the rock is undrained at this time. The pore water pressure is influenced by external loads and is not simply equal to the water pressure. Based on the pore elasticity theory, the pore water pressure P_w within the rock in an undrained state is related to the average stress P[54], with the calculation equation being:

$$P_w = \xi\left(\frac{\sigma_1 + \sigma_2 + \sigma_3}{3}\right) = \xi\left(\frac{\sigma_s + \sigma_d + 2\sigma_w}{3}\right) \tag{15}$$

In the equation, ξ is the Skempton coefficient.

Under the action of stresses σ_n and τ, the wedging force F_3 represents the sliding component parallel to σ_3 (resisted by the friction force between the crack surfaces), which acts on the midpoint of the main crack, resulting in the wing crack to open. This can be obtained from Eq. (16).

$$F_3 = 2a(\tau - f_d\sigma_n)\sin\phi \tag{16}$$

In the equation, f_d represents the coefficient of kinetic friction between the crack surfaces, assuming that the friction force is uniformly distributed across the crack surfaces, and $\tau - f_d\sigma_n$ represents the effective shear stress on the crack surfaces. The wedging force F_3 produces a stress intensity factor $K_{I(F)}$ at the tip of the wing crack, which can be obtained from Eq. (17)[55].

$$K_{I(F)} = \frac{2a(\tau - f_d\sigma_n)\sin\phi}{\sqrt{\pi l}} \tag{17}$$

Water pressure similar to confining pressure can restrain the propagation of wing cracks, while pore water pressure splitting can promote the propagation of wing cracks. Therefore, the stress intensity factor $K_{I(w)}$ at the end of the wing crack in the combined effect of pore water pressure and confining pressure can be determined using the following Eq. (18).

$$K_{I(w)} = -(\sigma_3 - p_w)\sqrt{\pi l} \tag{18}$$

Similarly, changes in temperature cause thermal expansion deformation of minerals within rocks. When the temperature T exceeds the threshold temperature T_e, the thermal expansion force generated by temperature transforms into structural thermal stress and acts on the periphery of wing cracks. Therefore, the structural thermal stress of rocks caused by temperature changes produces a stress intensity factor $K_{I(T)}$ at the ends of wing cracks. The specific calculation equation is determined by Eq. (19).

$$K_{I(T)} = \sigma_T\sqrt{\pi l} = \frac{E\alpha_T\Delta T}{1-\mu}\sqrt{\pi l}(T \geq T_e \tag{19}$$

In the equation, E and μ represent the elastic modulus and Poisson's ratio of the mineral grains, respectively, α_T represents the thermal expansion coefficient, and ΔT represents the temperature change value.

In the context of THM coupling, the crack-crack interaction should be taken into account in addition to the combined effects of external load, thermal expansion stress, and internal pore water pressure. For the rock material with multiple cracks, the internal micro-cracks continue to expand under the action of outer loads, and the rock bridge between cracks will be damaged. The adjacent cracks penetrate each other, resulting in the overall instability and failure. Combined with the calculation equation of thermal expansion stress σ_T[21], the calculation

equation of the average internal stress σ_3^i on the rock bridge with no crack ligament length $S-2(l+a\cos\phi)$ between the wing cracks in the σ_3 direction can be expressed as follows :

$$\sigma_3^i=\frac{F_3+\lambda P_w l+\sigma_T}{S-2(l+a\cos\phi)}=\frac{2a(\tau-f_d\sigma_n)\sin\phi+\lambda P_w l+E\alpha_T\Delta T l/(1-\mu)}{S-2(l+a\cos\phi)} \tag{20}$$

$$S=1/\sqrt{N_A}$$

where N_A represents the amount of compression-shear cracks per unit area.

Due to the existence of σ_3^i, there will be an additional stress intensity factor $K_{I(\sigma)}$, namely:

$$K_{I(\sigma)}=\frac{F_3+\lambda P_w l+\sigma_T}{S-2(l+a\cos\phi)}\sqrt{\pi l} \tag{21}$$

The dynamic stress intensity factor K_{Id} generated at the end of the wing crack propagation process under THM coupling and impact load conditions can be obtained by the simultaneous Eqs. (17), (18), (19) and (21), and K_{Id} is the only physical quantity that needs to be determined to characterize the stress field characteristics at the crack end.

$$K_{Id}=K_{I(F)}+K_{I(w)}+K_{I(T)}+K_{I(\sigma)}=\frac{2a(\tau-f_d\sigma_n)\sin\phi}{\sqrt{\pi l}}-(\sigma_3-p_w)\sqrt{\pi l}+\sigma_T\sqrt{\pi l}+\frac{F_3+\lambda P_w l+\sigma_T}{S-2(l+a\cos\phi)}\sqrt{\pi l} \tag{22}$$

Based on fracture mechanics criteria and using Eqs. (1) to (6) to solve Eq. (12), we can obtain the stress intensity factor expression for the interaction between rock wing cracks under THM coupling and impact load conditions:

$$K_{Id}=Ac_1\sigma_1-Bc_2\sigma_3+c_3p_w+\frac{E\alpha_T\Delta T}{1-\mu}c_4 \tag{23}$$

where:$A=\sin 2\phi\sin\phi-f_d\sin\phi(1-\cos\phi)$

$$B=\sin 2\phi\sin\phi+f_d\sin\phi(1+\cos\phi)$$

$$c_1=\frac{a}{\sqrt{\pi l}}+\frac{a\sqrt{\pi l}}{S-2(l+a\cos\phi)}$$

$$c_2=\frac{a}{\sqrt{\pi l}}+\sqrt{\pi l}+\frac{a\sqrt{\pi l}}{S-2(l+a\cos\phi)}$$

$$c_3=\sqrt{\pi l}-\frac{2af_d\sin\phi}{\sqrt{\pi l}}+\frac{\lambda l\sqrt{\pi l}}{S-2(l+a\cos\phi)}$$

$$c_4=\sqrt{\pi l}-\frac{\sqrt{\pi l}}{S-2(l+a\cos\phi)}$$

Under static loading, when the stress intensity factor is up to the static fracture toughness of the rock, cracks begin to develop and propagate within the rock, ultimately leading to macroscopic failure of the rock. Under impact loading, due to time-dependent processes near the crack tip, the dynamic fracture toughness is significantly larger than the static fracture toughness[56]. Therefore, microcracks in rock are less likely to propagate under dynamic loading, and a greater load is required to cause rock failure. This is also one of the primary causes of rock's greater dynamic strength than static strength. The dynamic stress intensity factor and dynamic fracture toughness at the crack tip are both time-dependent under dynamic loading since the load changes with time. Previous studies have shown that the two exhibit an exponential relationship[57]. Therefore, the crack propagation criterion for a dynamic slip-type crack model with multiple crack interactions can be calculated as:

$$K_{ID}(t)=1.917\left(\frac{dK_{Id}(\sigma,t)}{dt}\right)^{0.267} \tag{24}$$

In the equation, $K_{ID}(t)$ is the dynamic fracture toughness, $K_{Id}(\sigma,t)$ represents the dynamic stress intensity factor of the dynamic slip model of multiple crack interaction, which is mainly related to the applied stress σ and the load application time.

To calculate the K_{ID} and K_{Id} of rock under THM coupling and impact loading, the parameter values in Eq. (13) are as follows: $\sigma_3=\sigma_w=3$ MPa、 8 MPa and 14 MPa, coefficient of thermal expansion $\alpha_T=5\times10^{-6}$/K, modulus of elasticity $E=100$GPa, poisson ratio $\mu=0.4$, water wedge coefficient $\lambda=1.5$, $S=6$ mm, crack angle $\phi=45°$, coefficient of kinetic friction $f_d=0.75$, Initial crack length $a=1$ mm, General definition of normalized crack length $L=l/a=1$, Skempton coefficient ξ Affected by effective stress, changes occur depending on the axial static stress and water pressure exerted on the rock. The values of the Skempton coefficient of sandstone under various working conditions are listed in Table 6[6], $T=51℃$ and $57℃$, $\sigma_1=\sigma_s+\sigma_d$ includes dynamic loads σ_d that vary over time, calculated from transmitted wave, reflected wave, and incident wave data tested by

	ξ				
σ_s/MPa	σ_w = 3 MPa	σ_w = 5 MPa	σ_w = 8 MPa	σ_w = 11 MPa	σ_w = 14MPa
26	0.52	0.54	0.56	0.60	0.65

Table 6. Skempton coefficients for different conditions.

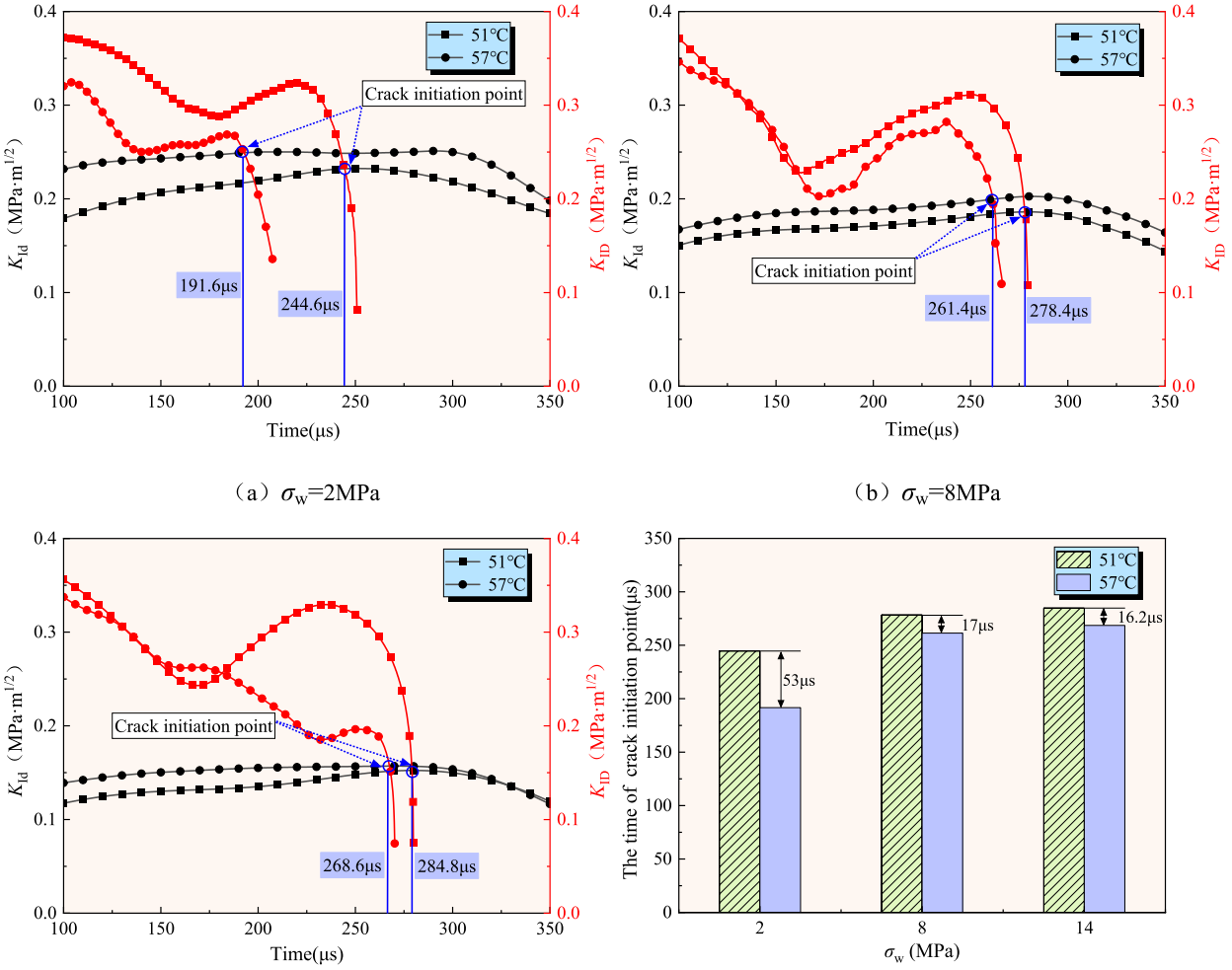

（a）σ_w=2MPa　（b）σ_w=8MPa

（c）σ_w=14MPa　（d）Time variation of crack initiation point

Fig.22. Curves showing changes in the K_{Id}, K_{ID}, and crack initiation time under THM coupling.

the SHPB data acquisition system. Substituting the above parameter values into Eqs. (13) and (14) yields the K_{Id} and K_{ID} as functions of temperature and water pressure, as listed in Fig. 22.

When the K_{Id} of rock pore cracks reaches the K_{ID}, i.e., when the K_{Id} curve in the figure is higher than the K_{ID} curve, cracks begin to development and propagation within the rock. The intersection point of the K_{Id} and K_{ID} curves in the figure represents the crack initiation point[58]. As seen in Fig. 22, under the same temperature conditions, as water pressure increases, the K_{Id} generally decreases, and the time at which cracks initiate is delayed. For example, at a temperature of 51 °C, when water pressure increases from 2 to 14 MPa, the time at which the crack initiation point appears is delayed from 244.6 μs to 284.8 μs. This explains that an increase in water pressure inhibits the development and propagation of microcracks within the rock. When water pressure is low, the pore cracks within the rock initiate and propagate first, ultimately leading to unstable failure. Water pressure plays an inhibitory role in the propagation of pore cracks.As can be depicted from Fig. 22, when the water pressure is the same, the dynamic stress intensity factor generally increases gradually as the temperature exceeds the threshold temperature. And the time at which cracks initiate occurs earlier. For example, when the water pressure is 2 MPa, 8 MPa, and 14 MPa, and the temperature increases from 51 °C to 57 °C, the time at which cracks initiate occurs earlier by 53 μs, 17 μs, and 16.2 μs, respectively. This is because high temperatures cause thermal cracking effects and pore water pressure degradation effects due to thermal

stress in the rock's internal structure, accelerating the initiation and propagation of microcracks within the rock, leading to an earlier onset of crack initiation. However, when water pressure is high, the variation in the time of crack initiation onset across different temperature conditions is not significant.Through computational analysis using the THM coupling and impact load-induced microcrack propagation model, it was found that the onset time of crack initiation and the K_{Id} in rock pores gradually delay and decrease with increasing water pressure, but gradually advance and increase with rising temperature. This suggests that the macro-scale damage extent of rock decreases gradually with increasing water pressure but increases gradually with rising temperature. The computational results are consistent with the failure patterns observed in experiments, where the extent of rock failure varies with water pressure and temperature. This validates the reliability of the THM coupling and impact load-induced microcrack propagation model. Therefore, the THM coupling and impact load-induced microcrack propagation model developed in this study can provide an effective reference for analyzing microcrack propagation and surrounding rock strength stability in complex deep underground environments in coal mines. The dynamic fracture toughness of sandstone under dynamic loading is different from its fracture toughness under static loading, even though the fact that the microcrack developed model in this study can represent the effects of temperature and water pressure variations on microcrack propagation within rocks. Currently, there is no unified physical–mechanical equation to determine the K_{ID} of sandstone. the K_{ID} of rocks is thought to show an exponential relationship with the rate at which the K_{Id} increases in the majority of investigations on rock dynamic fracture mechanics[59].Therefore, this study adopts the relationship equation between rock dynamic fracture toughness and dynamic stress intensity factor from Zhang Rongrong et al. Error! Reference source not found. to calculate the K_{ID} of rocks. In order to better understand how the K_{ID} changes with temperature and water pressure, as well as how THM coupling and impact loading conditions affect the dynamic microcrack propagation behavior of rocks, dynamic fracture mechanics experiments on sandstone under these conditions will be carried out in the future.

Conclusions

(1) Under THM coupling, the deep rock's dynamic stress–strain curve has nonlinear features and can be loosely divided into three stages: elastic deformation, plastic yielding, and post-peak failure. Among these, the plastic yielding stage is relatively long and resembles a "plastic plateau." Under the same water pressure, axial static stress, and impact load conditions, the energy time evolution distribution of deep rock during impact compression exhibits synchronous amplitude characteristics. Under the same temperature conditions, as water pressure increases, the energy reflection coefficient, energy transfer coefficient, and energy dissipation coefficient of deep rock exhibit exponential, linear, and Gaussian relationships with water pressure, respectively. Among these, the energy transfer coefficient primarily rises and then decreases with rising temperature.

(2) At the macro level, the dynamic failure patterns of rocks exhibit different modes with changes in temperature and water pressure, primarily categorized into three modes: compressive shear crushing failure, oblique shear boundary failure, and fracturing failure; At the micro level, for rocks that have not undergone compressive shear crushing failure, as water pressure rises, the dynamic damage variables gradually decrease. The dynamic damage threshold D_{cr} for deep sandstone ranges between 0.35 and 0.36, as evidenced by the decreasing opening width, extension length, and number of main cracks on the failure surface.

(3) At the microscopic level, as water pressure increases, the microstructure of rock fracture surfaces first exhibits intergranular fractures, which gradually develop into a composite type of fracture involving both intergranular and transgranular fractures, and finally manifest as transgranular fractures. The NMR test shows that rock internal pores gradually strengthen under water pressure, manifested as a decrease in pore diameter and a reduction in total porosity.

(4) Accurately reproduce the multi-field coupling state of the "three highs and one disturbance" in the deep subsurface, combined with the influence of hydrostatic confining pressure, pore water pressure, and temperature. A THM coupling and impact load-induced microcrack propagation model is proposed to investigate the dynamic stress intensity factor(K_{Id})and the crack initiation point changes in sandstone under impact load conditions in a THM-coupled environment. As pore water pressure increases, the K_{Id} gradually decreases, and the crack initiation time is delayed. However, when the temperature exceeds the threshold temperature, the crack initiation time gradually advances with increasing temperature, indicating that thermal damage accelerates the dynamic failure of rock.

Data availability

Data is provided within the manuscript.

Received: 4 November 2025; Accepted: 24 December 2025
Published online: 26 January 2026

References

1. Xie, H. et al. Study on the mechanical properties and mechanical response of coal mining at 1000 m or deeper. *Rock Mech. Rock Eng.* **52**, 1475–1490 (2019).
2. Zhou, H. W. et al. Acoustic emission based mechanical behaviors of beishan granite under conventional triaxial compression and hydro-mechanical coupling tests. *Int. J. Rock Mech. Min. Sci.* **123**, 104125 (2019).
3. Jia, Z. et al. Energy evolution of coal at diferent depths under unloading conditions. *Rock Mech. Rock Eng.* **52**, 4637–4649 (2019).
4. Zhang, A. et al. Mechanical properties and energy characteristics of coal at different depths under cyclic triaxial loading and unloading. *Int. J. Rock Mech. Min. Sci.* **161**, 105271 (2023).
5. An, H. & Xinghai, Mu. Contributions to rock fracture induced by high ground stress in deep mining: a review. *Rock Mech. Rock Eng.* **58**, 463–511 (2025).

6. Tan, T. et al. Mechanical behavior and damage constitutive model of sandstone under hydro-mechanical (H-M) coupling. *Int. J. Min. Sci. Technol.* **34**, 837–853 (2024).
7. Xie, H. et al. Experimental study on the mechanical and failure behaviors of deep rock subjected to true triaxial stress: a review. *Int. J. Min. Sci. Technol.* **32**, 915–950 (2022).
8. Duan, J. et al. Study on stress wave propagation and failure characteristics of key parts in tunnel under blasting load. *Scientifc Reports.* **14**, 29034 (2024).
9. Wang, Qi. et al. Dynamic mechanical characteristics and application of constant resistance energy-absorbing supporting material. *Int. J. Min. Sci. Technol.* **32**, 447–458 (2022).
10. Jun, Lu. et al. True triaxial experimental study of disturbed compound dynamic disaster in deep underground coal mine. *Rock Mech. Rock Eng.* **53**, 2347–2364 (2020).
11. Li jie Long, Dong yan Liu, Yan Xiang, et al. Coupling characteristics of permeability and volume strain of sandstone under seepage-stress coupling. *J Eng Sci Technol Rev.* **13**(4), 143–153 (2020).
12. Li, M. et al. Evaluating the pore characteristics of granite in disposal system under thermo-hydro-mechanical (THM) coupling. *Int. J. Rock Mech. Min. Sci.* **160**, 105237 (2022).
13. Feng, G. et al. Effect of thermal cycling-dependent cracks on physical and mechanical properties of granite for enhanced geothermal system. *Int. J. Rock Mech. Min. Sci.* **134**, 104476 (2020).
14. Freire-Lista, D. M., Fort, R. & Varas-Muriel, M. J. Thermal stress-induced microcracking in building granite. *Eng. Geol.* **206**, 83–93 (2016).
15. Tian, H. et al. Physical Properties of Sandstones After High Temperature Treatment. *Rock Mech. Rock Eng.* **45**(45), 1113–1117 (2012).
16. Hashiba, K. & Fukui, K. Effect of water on the deformation and failure of rock in uniaxial tension. *Rock Mechanics&Rock Engineering.* **48**(5), 1751–1761 (2015).
17. Jiefang, J. I. N., Juntao, S. U. N. & Honghao, Y. A. N. G. Experimental investigation of the influence of high water pressure on dynamic strength and deformation characteristics of red sandstone. *Chin. J. Rock Mech. Eng.* **42**(10), 2372–2384 (2023).
18. Cheng Han, Z. H. A. N. G. et al. Hydraulic properties and energy dissipation of deep hard rock under H-M coupling and cycling loads. *Therm. Sci.* **23**(S3), S943–S950 (2019).
19. Meng, T. et al. Evolution of the permeability and pore structure of transversely is otropic calcareous sediments subjected to triaxial pressure and high temperature. *Eng. Geol.* **253**, 27–35 (2019).
20. Long, L. J. et al. Mechanical properties of sandstone subjected to coupling of temperature-seepage-stress. *DYNA.* **96**(3), 309–315 (2021).
21. Ou Mi, Ru. et al. Mechanical properties and damage characteristics of granite surrounding rock in deep tunnel under thermal-hydro-mechanical coupling condition. *Tunn. Undergr. Space Technol.* **156**, 106262 (2025).
22. Xia, K. & Yao, W. Dynamic rock tests using split Hopkinson (Kolsky) bar system: A review. *J Rock Mechanics and Geotechnical Engineering.* **7**, 27–59 (2015).
23. Zhang, Q. B. & Zhao, J. A review of dynamic experimental techniques and mechanical behaviour of rock materials. *Rock Mech. Rock Eng.* **47**, 1411–1478 (2014).
24. Liu, K. et al. Dynamic mechanical and fracture behaviour of sandstone under multiaxial loads using a triaxial hopkinson Bar. *Rock Mech. Rock Eng.* **52**, 2175–2195 (2019).
25. Jin, J. et al. Determination and evolution of dynamic viscosity coefficient of rock under high water pressure and high-stress conditions. *Rock Mech. Rock Eng.* **58**(5), 4701–4718 (2025).
26. Bangbiao, Wu. et al. Dynamic compressive characteristics of a green sandstone under coupled hydraulic-mechanical loading: Experiments and theoretical modeling. *J Rock Mechanics and Geotechnical Engineering.* **17**, 126–138 (2025).
27. Wang, K. et al. Dynamic behaviour and failure mechanism of coal subjected to coupled water-static-dynamic loads. *Soil Dyn. Earthq. Eng.* **153**, 107084 (2022).
28. Zhao, G. et al. A modified triaxial split hopkinson pressure bar (SHPB) system for quantifying the dynamic compressive response of porous rocks subjected to coupled hydraulic-mechanical loading. *Geomechanics and Geophysics for Geo-Energy and Geo-Resources.* **8**(1), 2–15 (2022).
29. Chen, S. et al. In-situ stress measurements and stress distribution characteristics of coal reservoirs in major coalfields in china: implication for coalbed methane (CBM) development. *Int J Coal Geology.* **182**, 66–84 (2017).
30. Wu, X. et al. Variations of physical and mechanical properties of heated granite after rapid cooling with liquid nitrogen. *Rock Mech. Rock Eng.* **52**(7), 2123–2139 (2019).
31. Kim, T. & Jeon, S. Experimental study on shear behavior of a rock discontinuity under various thermal, hydraulic and mechanical conditions. *Rock Mech. Rock Eng.* **52**(7), 2207–2226 (2019).
32. Wang, Q. et al. Dynamic mechanical characteristics and application of constant resistance energy-absorbing supporting material. *Int J Mining Science and Technology.* **32**(3), 447–458 (2022).
33. Linming, D. O. U. et al. Mechanism of coakgas dynamic disasters caused by the superposition of static and dynamic loads and its control technology. *J. China Univ. Min. Technol.* **47**(1), 48–59 (2018).
34. Ulusay, R. *The ISRM suggested methods for rock characterization, testing and monitoring:2007–2014* 51–68 (Springer International Publishing, 2015).
35. Chinese Society of Rock Mechanics and Engineering. Rock dynamic characteristics test procedure (T/CSRME001–2019) 2019.
36. Guofeng, Y. U. et al. Big data prediction and early warning platform for floor water inrush disaste. *J China Coal Society.* **46**(11), 3502–3514 (2021).
37. Yongshui, K. A. N. G. et al. Investigation of combined step-wised support technology for precise intervention of surrounding rock structure for deep rock roadway. *Chinese J Rock Mechanics and Engineering.* **42**(11), 2682–2693 (2023).
38. Zhou, Z. et al. Dynamic response and energy evolution of sandstone under coupled static-dynamic compression: insights from experimental study into deep rock engineering applications. *Rock Mech. Rock Eng.* **53**, 1305–1331 (2020).
39. Han, Z., Li, D. & Li, X. Dynamic mechanical properties and wave propagation of composite rock-mortar specimens based on SHPB tests. *Int. J. Min. Sci. Technol.* **32**(04), 793–806 (2022).
40. Gao, X. & sheng Xue, Tu Qingyi.,. Study on dynamic compression characteristics of coal containing gas under different strain rates. *Sci. Rep.* **15**, 227 (2025).
41. Wu, Q. H. et al. Experimental investigation of the dynamic response of prestressed rockbolt by using an SHPB-based rockbolt test system. *Tunn. Undergr. Space Technol.* **93**, 103088 (2019).
42. Wang, H. et al. Experimental study on fractal dimension of energy dissipation and crack growth in saturated tuffated different strain rates. *Scientifc Reports.* **14**, 13338 (2024).
43. Huaqiao, Xu. et al. Dynamic mechanical behavior and energy dissipation characteristics of low-temperature saturated granite under cyclic impact loading. *Scientifc Reports.* **14**, 26840 (2024).
44. Beijing, X. I. E. et al. Dynamic failure characteristics of primary coal-rock combination under hydrostatic pressure. *J China Coal Society.* **48**(5), 2153–2167 (2023).
45. Jiefang, J. I. N. et al. Water pressure and axial static stress are influential factors on the evolution of impact energy and damage characteristics of red sandstones. *J. China Coal Soc.* **49**(11), 4441–4455 (2024).
46. Wang, H. F. et al. Thermal stress cracking in granite. *Int J Rock Mechanics and Mining Sciences & Geomechanics Abstracts.* **26**(5), 234 (1989).

47. Ren, F. & Liu, T. Dynamic characterization of pressurized coal under cyclic weak impact loading. *Scientifc Reports.* **15**, 18817 (2025).
48. Han, Z. Y., Li, D. Y. & Li, X. B. Dynamic mechanical properties andwave propagation of composite rock-mortar specimens based on SHPB tests. *Int. J. Min. Sci. Technol.* **32**(4), 793–806 (2022).
49. Zhu, J. et al. Failure analysis of water-bearing rock under direct tension using acoustic emission. *Eng. Geol.* **299**, 106541 (2022).
50. Zhang, R. et al. Experimental study on effect of freeze-thaw cycles on dynamic mode-I fracture properties and microscopic damage evolution of sandstone. *Eng. Fract. Mech.* **279**, 109043 (2023).
51. Gong, Y. et al. Evolution of pore structure and analysis of freeze damage in granite during cyclic freeze-thaw using NMR technique. *Eng. Geol.* **335**, 107545 (2024).
52. Song, Li. et al. Porosity and permeability models for coals using low-field nuclear magnetic resonance. *Energy&Fuels* **26**, 5005–5014 (2012).
53. Gu, H. et al. Dynamic response and meso-deterioration mechanism of water-saturated sandstone under different porosities. *Measurement* **167**, 108275 (2021).
54. Ashby, M. F. & Sammis, C. G. The damage mechanics of brittle solids in compression. *Pure Appl. Geophys.* **133**(3), 489–521 (1990).
55. ATKINSON B K. Introduction to fracture mechanics and its geophysical applications. Fracture Mechanics of Rock,1987:1–26.
56. Zhi, P. E. N. G. & xiong, ZENG Ya wu.,. Microcrack propagation-based damage mechanics model of rock. *J Northeastern University (Natural Science).* **43**(12), 1784–1791 (2022).
57. Bhat, H. S., Rosakis, A. J. & Sammis, C. G. A Micromechanics Based Constitutive Model for Brittle Failure at High Strain Rates. *J Appl Mechanies.* **79**(3), 3116 (2012).
58. Roman, Y. & Makhnenko, J. F. Elastic and inelastic deformation of fluid-saturated rock. *Philosophical Transactions of the Royal Society A: Mathematical, Physical and Engineering Sciences.* **374**(2078), 201504 (2016).
59. Cai, X. et al. Water saturation effects on dynamic behavior and microstructure damage of sandstone:Phenomena and mechanisms. *Eng. Geol.* **276**, 105760 (2020).
60. Wang, Ju. et al. Dynamic response of sandstone under hydro-mechanical coupling:macroscopic behavior and microscopic mechanism. *Int. J. Rock Mech. Min. Sci.* **197**, 106342 (2026).

Author contributions

Qi Ping: Writing – review & editing, Resources, Funding acquisition. Bobo Zhang: Writing–original draft, Validation, Methodology, lnvestigation, Formal analysis, Data curation, Conceptualization.

Funding

This work was supported by The National Natural Science Foundation of China (No.52074005, No.52074006),Qi Ping.

Declarations

Competing interests

The authors declare no competing interests.

Additional information

Correspondence and requests for materials should be addressed to B.Z.

Reprints and permissions information is available at www.nature.com/reprints.

Publisher's note Springer Nature remains neutral with regard to jurisdictional claims in published maps and institutional affiliations.